



Norwegian University of
Science and Technology

Influence on wind shear and turbulence in flow over obstacles

Jon Didriksen Guldsten

Master of Science in Product Design and Manufacturing

Submission date: June 2010

Supervisor: Per-Åge Krogstad, EPT

Problem Description

In large scale, high Reynolds number flows over bluff bodies the characteristics are influenced by geometry of the bluff body. Examples are pipelines lying on the sea floor and wind flow over hills. In the first case the separation of the flow from the surface of the body are important for both static and dynamic drag characteristics on the body. In the second case the shape of the body influences the developing flow over the body surface, which will have effects on the profiles of mean wind speed and turbulence. Such effects are important for choosing effective sites for wind turbines.

Flow phenomena as described above are often investigated using wind tunnels where one have to consider both the scaling problem (full scale versus laboratory scale) and the blockage problem in cases where experiment is performed in the test sections constrained by walls. A further challenge is to set up a realistic model of the full scale boundary layer entering the obstacles.

In this project both the scaling and blockage problems shall be addressed theoretically/ experimentally using wind tunnels and instruments that are available at the department.

Assignment given: 18. January 2010
Supervisor: Per-Åge Krogstad, EPT

EPT-M-2010-19/72

MASTER THESIS

for

Stud.techn. Gaizka Zarranandia and Stud.techn. Jon Guldsten
Spring 2010

Influence on wind shear and turbulence in flow over obstacles

Betydning for vindskjær og turbulens ved strømming over hindringer

In large scale, high Reynolds number flows over bluff bodies the flow characteristics are influenced by the geometry of the bluff body. Examples are pipelines lying on the sea floor and wind flow over hills. In the first case the separation of the flow from the surface of the body are important for both static and dynamic drag characteristics on the body. In the second case the shape of the body influences the developing flow over the body surface, which will have effects on the profiles of mean wind speed and turbulence. Such effects are important for choosing effective sites for wind turbines.

Flow phenomena as described above are often investigated using wind tunnels where one will have to consider both the scaling problem (full scale versus laboratory scale) and the blockage problem in cases where the experiment is performed in test sections constrained by walls. A further challenge is to set up a realistic model of the full scale boundary layer entering the obstacle.

In this project both the scaling and blockage problems shall be addressed theoretically/experimentally using wind tunnels and instrumentation that are available at the department.

-- ” --

Within 14 days of receiving the written text on the diploma thesis, the candidate shall submit a research plan for his project to the department.

When the thesis is evaluated, emphasis is put on processing of the results, and that they are presented in tabular and/or graphic form in a clear manner, and that they are analyzed carefully.

The thesis should be formulated as a research report with summary both in English and Norwegian, conclusion, literature references, table of contents etc. During the preparation of the text, the candidate should make an effort to produce a well-structured and easily readable report. In order to ease the evaluation of the thesis, it is important that the cross-references are correct. In the making of the report, strong emphasis should be placed on both a thorough discussion of the results and an orderly presentation.

The candidate is requested to initiate and keep close contact with his/her academic supervisor(s) throughout the working period. The candidate must follow the rules and regulations of NTNU as well as passive directions given by the Department of Energy and Process Engineering.

Pursuant to “Regulations concerning the supplementary provisions to the technology study program/Master of Science” at NTNU §20, the Department reserves the permission to utilize all the results and data for teaching and research purposes as well as in future publications.


One – 1 complete original of the thesis shall be submitted to the authority that handed out the set subject. (A short summary including the author’s name and the title of the thesis should also be submitted, for use as reference in journals (max. 1 page with double spacing)).

Two – 2 – copies of the thesis shall be submitted to the Department. Upon request, additional copies shall be submitted directly to research advisors/companies. A CD-ROM (Word format or corresponding) containing the thesis, and including the short summary, must also be submitted to the Department of Energy and Process Engineering

Department of Energy and Process Engineering, 12. January 2010



Olav Bolland
Department Manager



Per-Åge Krogstad
Academic Supervisor

Acknowledgements

This study has been carried out at the Department of Energy and Process Engineering at The Norwegian University of Science and Technology in the spring semester of 2010.

We would like to express sincere appreciation and gratitude to our supervisors Lars Sætran and Per-Åge Krogstad for their guidance and support throughout the research process. We also like to acknowledge Hrvoje Kozmar for his wise advises in the times when practical guidance was needed. We further wish to acknowledge the skilled laboratory technician Arnt Egil Kolstad for the help in the workshop. The last but not the least we want to thank Pål Egil Eriksen for sharing his wisdom about everything related to wind-tunnel experimenting.



Jon Didirksen Guldsten



Gaizka Zarraonandia Simeon

Trondheim, 14 June 2010

Abstract

A wind tunnel study of speed-up effects above the very crest of a sharp-edged escarpment and a hill peak in a simulated atmospheric boundary layer has been carried out.

It was desired to do a part-depth simulation of an atmospheric boundary that could be found above sea or coastal area exposed to the open sea. Because of the limited work section length it was used a modified roughness, barrier and mixing-device method developed by Counihan to accelerate the boundary layer growth. The mean velocity, integral length scales, power spectrum and turbulence intensity in the simulated boundary layer were compared with full scale empirical data. It showed good agreement except for the turbulence intensity which was too low.

Speed-up effects for the mean horizontal velocity and the longitudinal turbulence intensity above the very crest of an escarpment and a hill peak were investigated in the simulated atmospheric boundary layer. From the results it was observed that the speed-up effect gave a decrease in the turbulence intensity and a more uniform profile with height. In addition, it was observed a considerably increase of the horizontal mean velocity in the lowest part of the atmospheric boundary layer.

Scaled-up data from the wind tunnel experiment were compared with estimations from the Norwegian standard and potential flow with varying degree of agreement.

Sammendrag

En vindtunellstudie med fokus på akselerasjonseffekter i strømning over en fjelltopp og i overgangen mellom en skråning og et flatt platå i et simulert atmosfærisk grensesjikt har blitt gjennomført.

Det var ønsket å gjøre en simulering av den nederste delen av et atmosfærisk grensesjikt som var typisk for kystområder. På grunn av en begrenset vindtunell-lengde, ble det nødvendig å bruke en simuleringsmetode som var utviklet av Counihan til å akselerere veksten av grensesjiktet. Gjennomsnittshastighet, integral lengdeskalaer, "power spectrum" og turbulensintensiteten ble sammenlignet med empiriske data for et atmosfærisk grensesjikt og viste en akseptabel likhet. Eneste unntaket var turbulensintensiteten, som var noe lav.

Akselerasjonseffekten på den horisontale gjennomsnittshastigheten og turbulensintensiteten ble undersøkt over toppen av et fjell og i overgangen mellom en skråning og et flatt platå i det simulerte atmosfæriske grensesjiktet. Resultatene viste en lavere turbulensintensitet og en mer jevn profil med høyden. Det ble også observert en klar økning i den horisontale gjennomsnittshastigheten i den nedre delen av strømningen.

De oppskalerte dataene fra vindtunelleksperimentet ble sammenlignet med Norsk standard og potensialstrømning.

Contents

Acknowledgements	i
Abstract	iii
Sammendrag	iv
Contents	v
List of tables	ix
List of figures	x
Nomenclature	xii
Roman	xii
Greek letters	xiii
Abbreviations	xiv
1 Introduction	1
1.1 Facilities	1
1.2 Equipment	1
1.2.1 Calibration	3
1.2.2 Correction	4
2 The atmospheric boundary layer	5
2.1 Wind velocity profile in a neutral ABL	6
2.1.1 The log-law model	6
2.1.2 The power-law model	8
2.2 Turbulence in the ABL	8
2.2.1 Standard deviation of the velocity	9
2.2.2 Turbulence intensity	10
2.2.3 Roughness length and displacement thickness	11
2.2.4 Integral length scale	12
2.2.5 Turbulence spectrum	15
3 Wall bounded flow	19
4 Potential Flow	21
4.1 Flow around a cylinder	21
4.2 Panel method	23
5 The Norwegian Standard NS 3491-4	25
5.1 Equations of Norwegian Standard	25

6 Simulations in a wind tunnel	27
6.1 Similarity criteria for ABL simulating in a wind tunnel	27
6.2 Roughness, barrier and mixing –device methods	28
6.2.1 Short description of the hardware	29
6.2.2 Full depth and part depth simulations	29
6.3 Determination of the key parameters	29
6.4 Determination of the model scale-factor of the simulated ABL	30
6.4.1 Jensen’s number/model law	30
6.4.2 The method developed by Cook	30
6.4.3 The approach by Balendra	32
7 Experimental set up	33
7.1 Castellated barrier wall	33
7.2 The Spires	34
7.3 Fetch of roughness elements	35
7.4 Simulation over a cylinder	35
7.5 Simulation over a ramp	36
7.6 Blockage effect	36
8 Results	37
8.1 Artificial growth of the ABL	37
8.2 Similarity	37
8.2.1 Power-law and log-law fitting	39
8.2.2 Spectrum	40
8.2.3 Integral lengths	43
8.2.4 Roughness length	43
8.2.5 Roughness Reynolds number	43
8.2.6 Turbulence intensity	44
8.3 Flow over obstacles	44
8.3.1 Inflow Conditions; case 1	44
8.3.2 Velocity and fractional speed-up	46
8.3.3 Normalized standard deviation and local turbulence intensity	46
8.3.2 Inflow conditions; case 2: the hill	47
8.3.3 Comparison with Norwegian Standard	49
8.3.4 Comparison with potential flow	51

8.3.5 Pitot and hot wire disagreement.....	53
9 Conclusions	57
10 References	59
Appendix	63
A.1 Wind Tunnel Results	63
A.2 The wind tunnel results compared with the Norwegian Standard.....	64
A.3 The potential flow.....	66

List of tables

Table 1: Surface drag coefficient.	11
Table 2: Terrain categories in Eurocode1 [6].....	12
Table 3: Terrain categories by ESDU [28].....	12
Table 4: Constants used in the Norwegian Standard.....	26

List of figures

Figure 1: Boundary layer in the empty tunnel.....	2
Figure 2: Pitot tube and hot wire calibration curves.	3
Figure 3: Constants used in equation (2.20), proposed by Counihan [19].....	14
Figure 4: Verification of the different layers. Figure taken from <i>Fluid mechanics</i> book [40]	19
Figure 5: a) Source and sink locations. b) flow streamlines. Figure taken from <i>Fluid Mechanics</i> book [41].	21
Figure 6: Hill/escarpment.....	26
Figure 7: Wind tunnel arrangement sketch.	33
Figure 8: Dimensions of the barriers.....	34
Figure 9: Quarter-elliptic, constant wedge-angle Counihan spires	34
Figure 10: Half cylinder placed in the wind tunnel.....	36
Figure 11: Ramp dimensions.....	36
Figure 12: Picture of the 5 m of roughness fetch (left). Velocity profile of the empty wind tunnel.	37
Figure 13: Barrier, spires and roughness fetch installed in the wind tunnel.	37
Figure 14: Velocity profile of 3 and 4 spires.	38
Figure 15: Velocity profile at different lengths of fetch.	38
Figure 16: Velocity profile at the center and both sides.	39
Figure 17: Velocity profile at different velocities.....	39
Figure 18: Log-law and power-law fitting.	40
Figure 19: PSD and kaimal distribution.....	41
Figure 20: PSD of longitudinal velocity fluctuations at different heights and the correspondent Von Karman distribution.	41
Figure 21: PSD and kaimal distribution.....	42
Figure 22: PSD of longitudinal velocity fluctuations at different heights and the correspondent Von Karman distribution.	42
Figure 23: Integral length scales. For case 1 (right) and case 2 (left).....	43
Figure 24: Turbulence intensity. For case 1 (left), for case 2 (right).....	44
Figure 25: Velocity profile compared to the power-law (left). Turbulence intensity of the profile (right).	45
Figure 26: a) Mean horizontal velocity profile compared with the reference profile. b) Fractional speed-up (ΔS). c) The normalized standard deviation compared with the reference profile. d) Turbulence intensity compared with the reference profile.....	45
Figure 27: Velocity profile compared to the power-law (left). Turbulence intensity of the profile (right).	47

Figure 28: a) Mean horizontal velocity profile compared with the reference profile. b) Fractional speed-up (ΔS). c) The normalized standard deviation compared with the reference profile. d) Turbulence intensity compared with the reference profile.....	48
Figure 29: On set profile for case 1 a) and for case 2 b), compared with the profile law proposed in the Norwegian standard to represent the ABL.....	49
Figure 30: Mean horizontal velocity profile compared with the reference profile and fractional speed-up (ΔS) for; a) case 1 and b) case 2.	50
Figure 31: Mean horizontal velocity profile compared with the reference profile and fractional speed-up (ΔS) for case 1.....	51
Figure 32: a) Streamlines of the flow over the cylinder. b) On-set profile compared to the profile over the cylinder and two potential flow solutions. c) Speed-up ratio of the experiment and the potential flow solution. Where $H=62\text{mm}$ is the radius of the cylinder and $U_{\text{ref}}=11.3813\text{m/s}$	52
Figure 33: Pitot and hot wire disagreement.	53
Figure 34: Separation line of the cylinder.....	54
Figure 35: a) Hot wire in 0° and 90° configurations. b) mean velocity profile.	54
Figure 36: representation of the wake downwind the cylinder.....	55
Figure 37: a) Measured Pitot pressures. b) mean velocity profile.	55
Figure 38: Pressure field form potential flow solution [43].....	56
Figure 39: The results for case 3 and 4; a) Mean horizontal velocity profile compared with the reference profile. b) Fractional speed-up (ΔS). c) The normalized standard deviation compared with the reference profile. d) Turbulence intensity compared with the reference profile.....	63
Figure 40: Measured undisturbed mean velocity profile compared with the Norwegian Standard.....	64
Figure 41: Case 3 compared with the “Norwegian Standard” for; a) the mean horizontal velocity at the hill peak, b) the fractional speed-up.....	65
Figure 42: Case 4 compared with the “Norwegian Standard” for; a) the mean horizontal velocity at the hill peak, b) the fractional speed-up.....	65
Figure 43: Mean horizontal velocity profile compared with the reference profile and fractional speed-up (ΔS) for case 3.....	66
Figure 44 : Mean horizontal velocity profile compared with the reference profile and fractional speed-up (ΔS) for case 4.....	66

Nomenclature

Roman

\tilde{u}	fluctuating term of longitudinal velocity component
ℓ	mixing length
a	cylinder radius
d	displacement length
e	unamplified voltage
E	voltage
e_{corr}	corrected unamplified voltage
f_L	non-dimensional frequency
f_M	peak frequency
f_z	reduced frequency
g	Earth's gravity constant (9.8m/s^2)
H	obstacle height
h_f	height of the column of calibrating fluid
I	electrical intensity
I_u	turbulence intensity
K	surface drag coefficient
L_u^x	integral length of u velocity component in x direction
n	frequency
N_s	number of samples
R	electrical resistance
R_{20}	electrical resistance of the hot wire at 20°C
R_{total}	electrical resistance of the hot wire and the cable

T	current temperature
t	time
T	time period
T_w	working temperature of the wire
T_0	temperature of the ambience
u	instantaneous longitudinal velocity component
U	mean longitudinal velocity component
u^*	shear velocity
U_∞	free-stream velocity
U_{ref}	reference velocity
x	longitudinal length
y	horizontal length
z	vertical length, height
z_0	roughness length
z_{ref}	reference height
ΔP	pressure difference

Greek letters

ν	kinematic viscosity
α	power-law exponent
α_{20}	temperature coefficient of resistance
κ	Von Karman constant (0.41)
λ	latitude
ρ_{air}	density of air
ρ_f	density of calibrating fluid
σ_u	standard deviation of the longitudinal velocity component

τ	time differential
τ_0	surface shear stress
τ_{xz}	momentum stress
Ω	angular velocity of Earth

Abbreviations

2D	Two-dimensional
3D	Three-dimensional
ABL	Atmospheric Boundary Layer
ESDU	Engineering Sciences Data Unit
FFT	Fast Fourier Transform
PSD	Power Spectral Density

CHAPTER 1

1 Introduction

The wind flows over different terrain has been investigated for many years in full scale measurements, numerical simulations and wind tunnel experiments. It is of great importance in many engineering areas as for example pollution control, wind turbine siting and large civil engineering constructions. Despite the use of numerical methods in the estimation of wind flow in different terrains, the results of those simulations as every other numerical model need to be verified in real physical experience.

In this project it has been simulated a natural atmospheric boundary layer for later experiencing of how it would behave when obstacles are in its path. The obstacles simulate natural hills and escarpments, for convenience the hills are downgraded to basic forms of ramps and cylinder. The characteristics that these obstacles induce in the flow have a large importance for choosing effective sites for wind turbines.

1.1 Facilities

One of the NTNU wind tunnels was used for this project, usually used for natural boundary layer experiencing. It operates in a closed circuit mode and the working section is 1m wide, 0.5 m high and 7 m long. The airflow is achieved by an axial flow fan driven by an electrical motor. It is possible to change the air velocity from near zero and up to 30 m/s in continuity by controlling the relative positions of the fan vanes by rotating them.

1.2 Equipment

The measuring equipment used for the simulations consisted of Pitot tubes (that actually consist of Prandtl tubes) and hot wires (that work at constant temperature, not constant current type) for anemometry, connected to a pressure transducer in the case of the Pitot and then to amplification box as well as the hot wire. Data from the two anemometers was collected by a National Instruments NI cDAQ-9172 for a total time of 10 seconds and sampling frequencies of 500 Hz for the Pitot and 13 kHz for the hot wire (with a filter for frequencies at 6.5kHz). Labview was used to control the data acquisition instruments from the PC.

The Pitot tubes were chosen because of the easiness to handle, calibrate and the accuracy ratio to measure the average wind speeds to calculate the profile of the boundary layer, a hot wire anemometer was chosen to measure the wind speed variation because it is able to perform the measurements at a much higher frequency than the Pitot tube is, and it allows the user to know the turbulence content of the developed profile in the wind tunnel. It should be pointed out that the hot wire is far more complex to handle and delicate than the robust Pitot tube.

The temperature of the hot wire anemometer is chosen to be set at 250° C which is below 300°C as recommended for use in this type of simulations. This temperature is meant to be constant. The resistance of the wire is dependent on the temperature. As more air passes the wire, more heat is exchanged with the surrounding air and hence the resistance is changed. As the resistance changes an adjustment in current is required until new equilibrium is reached. The principle is that the temperature is measured in terms of electrical resistance; the current through the wire is adjusted as to keep constant temperature in the wire [20].

The resistance of the hot wire is calculated with the individual parameters of it and the following equation.

$$R = R_{total} + \alpha_{20} R_{20} (T_{sensor} - T_0) \quad (1.1)$$

Where R_{total} is the sum of the resistance of the hot wire itself, its holder and the link cable, T_w is chosen to be 250°C and T_0 is the calibration temperature. The rest of the parameters are depending on each wire. In these experiments α_{20} is 0.36 % and R_{20} (the resistance of the wire at 20°C) is 3.6 Ω . The R that is obtained through this formula is set as a constant operational resistance in an amplification box. The electrical intensity is the changing parameter, but the magnitude to be recorded is the voltage E .

$$E = I \cdot R \quad (1.2)$$

For the hot wire calibration the free stream section in the wind tunnel has been used, far from the boundary layers developed along the roof, walls and floor of the wind tunnel. A run was made with an empty tunnel in order to map the areas where the flow was disturbed by these boundaries. As it can be seen in figure 1, undisturbed flow is achieved from 100 mm to 250mm thus the calibration of both the Pitot and hot wire should be done in this range of height. It should be noted that the boundary layer along the floor is higher due to the rough fetch that was installed for the simulation of the boundary layer.

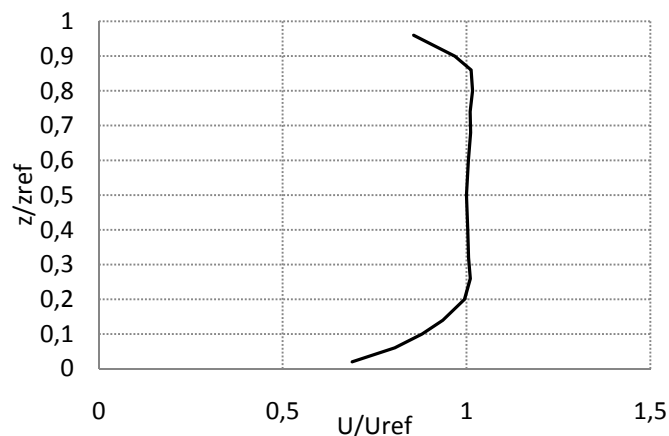


Figure 1: Boundary layer in the empty tunnel.

1.2.1 Calibration

The calibration was done at the same time for the two anemometers; 8 points were done at different flow velocities (between 3 m/s and the maximum desired velocity) and at every time the speed was compared with a sloped fluid column type manometer that was used as the reference speed through the following equation.

$$U = \sqrt{\frac{2\rho_f g h_f}{\rho_{air}}} \quad (1.3)$$

Where ρ_f and h_f are the density and column height, respectively, of the fluid in the manometer.

The calibration curve of the Pitot tube was fitted to a linear trend putting the pressure difference as a function of the voltage. The hot wire was fitted to a third degree polynomial because of its non-linearity, although a fourth degree one is also possible to use. As it is mentioned in the book by Doebelin [20] it can be possible to use an electrical linearizer, whose job would be to automatically produce this polynomial. In this case it was put directly the velocity in function of the voltage. The velocity for the Pitot is obtained through the following equation.

$$U = \sqrt{\frac{2\Delta P}{\rho_{air}}} \quad (1.4)$$

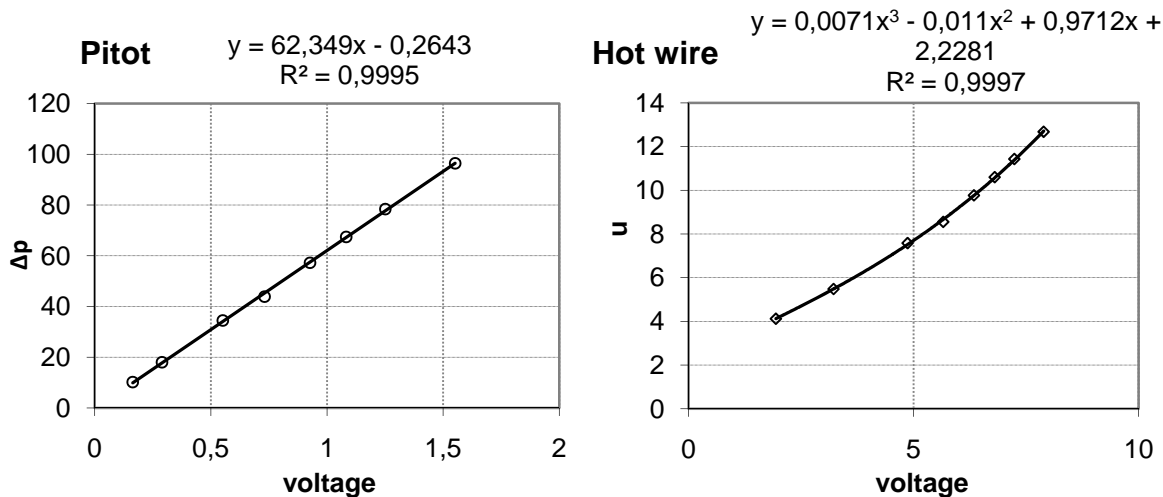


Figure 2: Pitot tube and hot wire calibration curves.

For the hot wire it was also needed to take into account the temperature of the air in the tunnel during the calibration and the later measurements during the simulations. Knowing that the basic of its work is to maintain a constant temperature of the wire, the slightest variation of the temperature of the surrounding air might affect the output. Initially the hot wire was fitted to the temperature of the first calibration point and later all the measured points were

corrected for this first temperature. This is done due to the temperature changes during the simulations, probably because of the heat of the electrical motor fan exchanged to the air flow inside the tunnel.

1.2.2 Correction

The output voltage must be corrected for the temperature changes through this equation.

$$e_{corr} = e \sqrt{\frac{T_w - T_0}{T_w - T}} \quad (1.5)$$

Where e and e_{corr} are the voltage and the corrected voltage respectively, and T_w , T_0 and T are the temperatures of the wire, the first calibration point and the actual temperature respectively.

After every experiment the hot wire was checked for the drifting of velocities. An error of 1% was valid.

CHAPTER 2

2 The atmospheric boundary layer

The nearest layer of the earth's surface is called the troposphere and extends from the ground to an average altitude of 11 km. Closest to the earth surface is the atmospheric boundary layer (also called the planetary boundary layer), which is defined as the part of the troposphere that is directly influenced by the earth's surface, and responds to surface changes with a timescale of about an hour or less. Above the atmospheric boundary layer is the free atmosphere where the wind is approximately geostrophic. The Atmospheric Boundary Layer (ABL) is a layer of air covering the earth, the thickness of which is determined by the height at which surface friction no longer affects the general flow of wind around the globe. Air in motion can be divided into two; the main flow, where viscosity (fluid friction) plays a negligible part, and the boundary layer flow where fluid friction is influential. The boundary layer is adjacent to a surface such as the surface of a planet [39].

The principal properties of the ABL that help to mainly describe it are: thermal stability, thickness of the layer (distance from the earth where the main flow is achieved), turbulence level, and mean wind velocity profile. The main effects that influence on the ABL's properties are the thermal effects, the characteristics of the geostrophic wind, the surface roughness and the Coriolis force.

The surface layer is 2D in nature but the Coriolis effects result in a 3D velocity field in the so-called Ekman spiral. This spiral shows the deflection of surface currents as the flow direction rotates during the descent from the top of the layer. In other words, the direction of the wind near the surface is completely different to the direction of the geostrophic wind (above the layer) because the Coriolis force makes the flow rotate.

There are three different types of thermal effects that are used to describe the thermal stability of the ABL: stable, unstable and neutral [7,32].

Unstable ABL: An ABL is unstable when the air is massively heated by the earth's surface through convection and causes the air near the surface to rise. As the air rises, the pressure around it decreases and hence the air gradually expands and cools adiabatically. It can occur that the heating is so large that the cooling process along the rising of the air is not enough, and the rising hot air continues to rise instead of getting into equilibrium with the surrounding air producing large convection cells. The result is a thick boundary layer with large-scale turbulent eddies. There is a high transfer of momentum, massive vertical mixing, and small changes in mean wind speed over the height of the layer are obtained. Here the turbulence has a thermal source.

Stable ABL: If the rising air gets colder (due to the adiabatic cooling) than the surrounding air, it is known as stable stratification. In this case, the vertical motion of the rising air will be

suppressed as the adverse temperature gradient makes it impossible. This is often the case of the ABL in night conditions when the surface of the earth is cooling down due to the lack of solar radiation. In this kind of stability situation, turbulence is dominated by friction with the surface, and the mean wind velocity changes with altitude are large. Here the turbulence has a mechanical source.

Neutral ABL: In the neutral atmosphere, with adiabatic lapse rate and no convection, air will remain in equilibrium with the surrounding along the whole ABL height. The neutral ABL is divided into three different layers. The lowest few centimeters of air is the micro layer or interfacial layer, where molecular transport dominates over turbulent transport. Above the micro layer is the surface layer, also called the logarithmic layer where the Coriolis and pressure forces can be neglected. Here, the wind has a constant direction and the velocity is horizontal. Above the surface boundary layer is the Ekman layer. In this layer the wind direction is not constant because it tends towards the geostrophic wind direction. This leads to the so-called Ekman-spiral. The ABL can be assumed neutral over sea, in strong wind or when it is a high density of clouds, when there is enough mixing. Usually this is the type of stability used for wind energy simulations.

The ABL layer's height is the distance between the surface of the earth and the main flow. The factor determining these two zones is that inside the layer, changes in wind velocity and exchange of momentum occur [7].

In the neutrally stable ABL, turbulence is the main cause of the thickness of the layer and turbulence is caused by surface roughness, so the more surface roughness the thicker the boundary layer. For example over large bodies of water the boundary layer height may be as low as 200 meters (due to the fact that water is a smooth surface), while above large cities it may be as high as 600 meters (buildings are big obstacles for wind flow making the surface to be very rough) [7]. In articles in which the experiments are very similar to the experiment in this project [2,28], refer to Counihan's review [19] and agree in a 500 m high standardized or recommended value for the ABL (for rural terrain).

2.1 Wind velocity profile in a neutral ABL

There are two main methods for describing the mean horizontal wind profile in the neutral ABL, the logarithmic law and the power-law.

2.1.1 The log-law model

The log-law can be derived from mixing length theory, eddy viscosity theory or similarity theory.

The log-law meets the lower boundary conditions of the atmospheric layer (velocity equals zero when height equals zero), but does not meet an upper boundary layer condition. The law fits best for z less than 100-150 meters.

Mixing length analysis given by Wortman in 1982 [32]:

Near the surface of the earth the momentum equation is reduced to:

$$\frac{\partial p}{\partial x} = \frac{\partial}{\partial z} \tau_{xz} \quad (2.1)$$

The pressure near the surface is independent of z and integration gives:

$$\tau_{xz} = \tau_0 + z \frac{\partial p}{\partial x} \quad (2.2)$$

The pressure gradient is close to zero near the surface and can therefore be neglected. Using the Prandtl mixing length theory, the shear stress can be written as:

$$\tau_{xz} = \rho \ell^2 \left(\frac{\partial U}{\partial z} \right)^2 \quad (2.3)$$

For the flow near a surface, Prandtl argued on dimensional reasoning that the mixing length is proportional to the distance from the surface and therefore $\ell = \kappa z$. The friction velocity is defined as:

$$u^* = \sqrt{\frac{\tau_0}{\rho}} \quad (2.4)$$

With the definitions of ℓ and u^* , and combining the two equations it can be written:

$$\frac{\partial U}{\partial z} = \frac{1}{\ell} \sqrt{\frac{\tau_0}{\rho}} = \frac{u^*}{\ell} \quad (2.5)$$

The integration of the equation from lower limit z_0 and zero velocity (Use z_0 instead of zero because the natural surfaces are never uniform smooth) to z and U :

$$\int_0^U \partial U = \frac{u^*}{\kappa} \int_{z_0}^z \frac{\partial z}{z} \quad (2.6)$$

The final result is the log-law:

$$U(z) = \frac{u^*}{\kappa} \ln \left(\frac{z}{z_0} \right) , z \geq z_0 \quad (2.7)$$

Tables and graphs of the z_0 can be found in many different articles as will be shown later. The log-law is often made use of to estimate the mean velocity at an exact height from the reference height and reference mean velocity:

$$\frac{U(z)}{U(z_r)} = \ln\left(\frac{z}{z_0}\right) / \ln\left(\frac{z_r}{z_0}\right) \quad (2.8)$$

It is accepted by many authors that the log-law does not represent the mean velocity profile at large heights, here the authors differ in the range of application; as Cook says [14] the log-law represents the lower 200 m, on the other hand Counihan [19] says that only the lower 30-50 m are represented by this law. It might seem after reading a number of articles that the limit proposed by Counihan is more accepted.

2.1.2 The power-law model

The power-law is an empirical equation describing the mean velocity profile. The law does not meet the lower boundary conditions (no slip at the earth's surface) and has also no upper boundary. Due to this, the law gives a poor fit for the lowest part of the ABL, but it gives a good estimate for the range 30-300 meters [14]. Counihan [19] says that the power-law gives a better fit to most of the data over a greater height range, and also for high wind conditions.

The equation:

$$\frac{U(z)}{U_{ref}} = \left(\frac{z}{z_{ref}}\right)^\alpha \quad (2.8)$$

U_{ref} is the mean wind velocity at a given reference height z_{ref} . The exponent α is mainly dependent on the surface roughness of the location, but also the wind speed and height-range of fit. Different exponents can be found in tables which they are obtained from experiments in real atmospheric data for different terrains.

2.2 Turbulence in the ABL

Another of the basic features of the ABL is its turbulence. There are two sources of turbulence in the layer; mechanical and thermal. Mechanical turbulence is induced by the velocity gradient along the height of the layer and thermal turbulence is due to the vertical temperature gradient in the atmosphere and it depends on the time of the day, as during the day the earth's surface is heated by the radiation from the sun, and in the night the earth is cooled. For wind velocities under approximately 10 m/s the thermal effects should not be ignored, thus for higher velocities mechanical characteristics are much more relevant [21].

The basic nature of turbulent flow is that the describing parameters are not constant with respect to time at fixed points in space; in fact they fluctuate through a wide range of frequencies. Motion in a turbulent flow is chaotic, fluid particles move randomly and their line paths match each other forming non-periodic vortexes. Although turbulent flow obeys the physical laws of conservation of mass, momentum and energy it is difficult to describe temperature, pressure, density and humidity as well as the motion of the air itself in three dimensions, as small changes in initial conditions may induce large differences in the later estimations. Indeed due to this chaotic characteristic it is more useful to analyze the turbulence in terms of statistics [21].

These main statistical properties are wind speed fluctuation frequency (turbulence spectra), turbulence intensity, autocorrelation, and integral time/length scale [32].

Turbulent wind consists of longitudinal, lateral and vertical components and is described by all the fluctuations in these three directions with frequencies higher than the variations of mean wind speed. Therefore, for the longitudinal component (the main flow speed) the total speed or instantaneous speed $u(z,t)$ is conceived as the sum of the short term mean speed $U(z,t)$ calculated over 10 minutes, and the fluctuating term $\tilde{u}(z,t)$, as well as the lateral and vertical components are calculated in the same way [32].

$$u(z,t) = U(z,t) + \tilde{u}(z,t) \quad (2.9)$$

The mean velocity $U(z,t)$ is referred to as the average value of the longitudinal component measured over a short period of time, usually 10 minutes [32].

$$U = \frac{1}{T} \int_0^T u(t) dt \quad (2.10)$$

But, however turbulent wind is not observed in the continuum, despite a number N_s of measurements of this speed u_i are taken at a certain sampling rate δt such that $\Delta t = N_s \cdot \delta t$. Then the short term mean is calculated:

$$U = \frac{1}{N_s} \sum_{i=1}^{N_s} u_i \quad (2.11)$$

2.2.1 Standard deviation of the velocity

Another important parameter to calculate is the standard deviation of the wind velocity which is defined as

$$\sigma_u^2 = \frac{1}{T} \int_{t_0-T/2}^{t_0+T/2} [u(t) - U]^2 dt \quad (2.12)$$

Or in the sampled form (usually the sampling rate is no less than 1Hz). In the experiments in this project the hot wire was used due to its resolution and the capability to work at high frequencies allowing for a clear pattern to calculate standard deviation, usually at a sampling rate of 13 kHz.

$$\sigma_u^2 = \frac{1}{N} \sum_{i=1}^N (u_i - U)^2 \quad (2.13)$$

It is a fact that the standard deviation is nearly constant up to the height of the usual wind turbines which are about 100 or 200 meters high for homogeneous terrain. These are the three deviation components of the turbulence

$$\sigma_u = 2.5u^* \quad \sigma_v \approx 0.75\sigma_u \quad \sigma_w \approx 0.5\sigma_u \quad (2.14)$$

This simple definitions of standard deviations are made for very low height, almost at ground level [21].

2.2.2 Turbulence intensity

Turbulence intensity is the ratio of the standard deviation of the wind speed σ_u over the mean \bar{u} and is telling where the major fluctuations of speed take part. Both deviation and mean speed are calculated over a period of time longer than the longest turbulent fluctuation; however this time is set to ten minutes by convention in wind energy engineering in the atmospheric measurements [32].

$$I_u(z) = \frac{\sigma_u}{U(z)} \quad (2.15)$$

There are different empirical formulations to approach the turbulence intensity. A simple one is to use a logarithmic approach assuming $\sigma_u/u^*=2.5$, where z_0 is the roughness length [21].

$$I_u(z) = \frac{1}{\ln\left(\frac{z}{z_0}\right)} \quad (2.16)$$

An alternative proposed by Walshe uses a surface drag coefficient depending on the terrain category [2].

$$I_u(z) = 2.58K^{0.5} \left(\frac{10}{z}\right)^\alpha \quad (2.17)$$

Where z is the height, α is the power-law coefficient and K is the surface drag coefficient which is given in the table 1.

In ESDU85 a formula for standard deviation for employing in turbulence intensity calculation is proposed.

$$\begin{aligned}\sigma_u &= \frac{7.5\eta(0.538+0.09\ln(z/z_0))^p u^*}{1+0.156\ln(u^*/fz_0)} \\ \eta &= 1-6fz/u^* \\ p &= \eta^{16} \\ f &= 2\Omega\sin(|\lambda|)\end{aligned}\tag{2.18}$$

Where Ω is the angular velocity of Earth and λ is the latitude of the location.

Terrain category	α	K
Open terrain with very few obstacles; e.g. open sea, farmland, desert, etc.	0.16	0.005
Terrain uniformly covered with obstacles 10-15m in height; e.g. small town, woodlands, etc.	0.28	0.015
Terrain with large and irregular objects; e.g. centres of large cities	0.40	0.05

Table 1: Surface drag coefficient.

The standard deviation σ_u is nearly constant all along the height of the ABL for the longitudinal component of the turbulence, and is approximated to $2.5u^*$ close to the ground [7]. Unlike the velocity profile, the turbulence intensity decreases with height, this is the case where the highest intensity takes place at the lowest wind speeds; nevertheless the height where this maximum is achieved depends somehow on the terrain roughness features. Turbulence intensity increases with terrain roughness and decreases with height.

2.2.3 Roughness length and displacement thickness

It can be said that the most characterizing parameter of a profile could be the roughness length which is creating the turbulence and thus the boundary layer itself, profile and height of it. A definition of z_0 could be “the height above the ground at which the mean wind velocity is zero”[21]. Authors agree on dividing the terrain into different categories depending on its roughness, so each of them give a roughness length depending on the surface material that go from smooth to rough terrain e.g: plane ice, open sea, coastal areas, and open land. The data might vary slightly from one source to another but they in spite of this they have a good agreement. Tabulated values can easily be found in the references [6,7,14,19,21,28,30,42].

Terrain category		z_0 m
0	Sea or coastal area exposed to the open sea	0,003
I	Lakes or flat and horizontal area with negligible vegetation and without obstacles	0,01
II	Area with low vegetation such as grass and isolated obstacles (trees, buildings) with separations of at least 20 obstacle heights	0,05
III	Area with regular cover of vegetation or buildings or with isolated obstacles with separations of maximum 20 obstacle heights (such as villages, suburban terrain, permanent forest)	0,3
IV	Area in which at least 15 % of the surface is covered with buildings and their average height exceeds 15 m	1,0

Table 2: Terrain categories in Eurocode1 [6]

In addition to the roughness length there is the parameter d which represents the displacement thickness. One definition is that when roughness elements are closely located to each other the whole roughness surface acts like it has been raised up the distance d from the ground [21,6]. There can be found tabulated values that relate the terrain categories, thus roughness length with the displacement length, which in smooth terrains results to be negligible [28].

Type of terrain		z_{0p} , m	d_p , m
(a)	Small towns	0.3	5 to 10
	Suburbs of large towns and cities		
	Wooded country (many trees)		
(b)	Outskirts of small towns	0.1	0 to 2
	Villages Countryside with many hedges, some trees and some buildings		
(c)	Open level country with few trees and hedges and isolated buildings; typical farmland	0.03	0
(d)	Fairly level grass plains with isolated trees	0.01	0

Table 3: Terrain categories by ESDU [28]

2.2.4 Integral length scale

The autocorrelation function $\rho_u^T(z, \tau)$ indicates in a turbulent flow the amount of information that a measurement of the speed component $u(x, y, z, t)$ will give about a future value in $t + \tau$ time of the same component $u(x, y, z, t + \tau)$. In other words, it is the amount of certainty that is disposed to make assumptions over time when a velocity component is known. Logically this amount of information decreases as the forecast time increases until its value is zero. That is when a component $u(x, y, z, t)$ is not able to give any information for predictions [21].

The two parameters that define the autocorrelation function are the height above the ground and the time difference or lag, z and τ respectively. Due to the assumption of a homogeneous horizontal flow, this is the main flow over the longitudinal axis. A measure of the average time that speed fluctuations are correlated, what some authors mention as a characteristic time of memory, is the time scale $T(z)$. This scale means that u measurements

give a high amount of information at a time τ if $\tau \ll T(z)$, but almost no information if $\tau \gg T(z)$ [21]. The turbulence integral time scale is defined as

$$T(z) = \int_0^{\infty} \rho_u^T(z, \tau) d\tau \quad (2.18)$$

To continue with the integral scales, the integral length scales are the measures of the vortices in the flow, in other words the average sizes of the gusts in a given direction. They depend on the height above the ground and on the roughness of the terrain; in addition wind velocity may also have an influence on them. In conclusion, the integral length scale is more representative of a site rather than the integral time scale, due to their tendency to be more constant over a range of wind speeds [21].

For example, L_u^x the integral length scale for the component u measured in the direction x .

$$L_u^x = \int_0^{\infty} \rho_u^T(z, \tau) d\tau \quad (2.19)$$

Each turbulence component has three scales, one for each direction.

$$\text{For } u: \quad L_u^x \quad L_u^y \quad L_u^z$$

$$\text{For } v: \quad L_v^x \quad L_v^y \quad L_v^z$$

$$\text{For } w: \quad L_w^x \quad L_w^y \quad L_w^z$$

There are also empirical formulas that estimate the longitudinal integral length scale, and often the remaining integral length scales are expressed as a function of this [21]. One is the proposed by Counihan in 1975 [19,21] for longitudinal integral length scales in the range of 10 to 240 m

$$L_u^x = Cz^{1/n} \quad (2.20)$$

Where the coefficients C and $1/n$ depend on the roughness length z_0 .

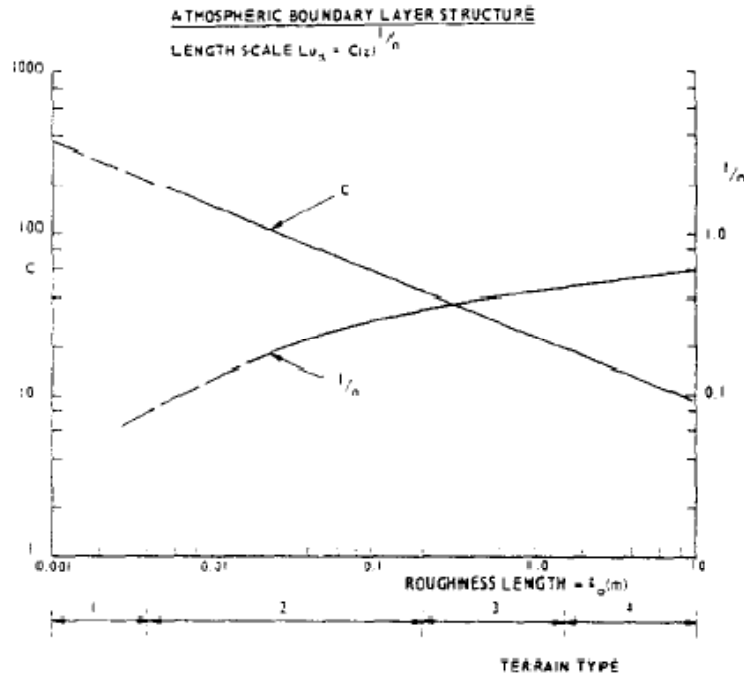


Figure 3: Constants used in equation (2.20), proposed by Counihan [19]

Although there is not any consensus in how the length scale grows, most authors now coincide in the fact that there is no growing above 200-300 m of the ground [19]. Also widely accepted is the formula by ESDU

$$L_u^x = 280 \left(\frac{z}{z_i} \right)^{0.35}$$

$$z_i = 1000 z_0^{0.18} \quad (2.21)$$

Where z_i is the length which separates the layer with growing integral length scales ($z < z_i$) and constant length scales ($z \geq z_i$) $L_u^x = 280$ m.

Such is the difference between proposed empirical formulas that they even express the opposite, for example as it is said in the book by Dyrbye et al. [21] “according to Counihan, integral length scales decrease with increasing surface roughness” and “the opposite variation is specified by ESDU”. This leads to untrustworthiness of these formulas.

Formulation proposed by Eurocode1, is often used in construction but not normally used in wind engineering [7]. It is also said that for using with the Kaimal spectrum the integral length scale must be multiplied by 1.7.

$$L_u^x = 300 \left(\frac{z}{300} \right)^\varepsilon \quad (2.22)$$

Where the exponent ε varies from 0.13 over open water to 0.46 over urban areas.

There are also simpler expressions as Danish standard and IEC [7] for Kaimal spectrum.

$$L_u^x = 150 \quad \text{and for } z < 30\text{m} \quad L_u^x = 5z$$

And IEC expression (slightly different)

$$L_u^x = 170.1 \quad \text{and for } z < 30\text{m} \quad L_u^x = 5.67z$$

With all this empirical formulae and the notations, no clear judgement can be done. The fact is some expressions fit better than others so there is no clear good and bad results evaluation. In particular, the results of the experiments done in this project fit to the best to the expression proposed by Walshe, used by Balendra et al. [2] and articles related to National University of Singapore that unfortunately could not be referenced.

$$L_u^x = 101 \left(\frac{z}{10} \right)^\alpha \quad (2.23)$$

Where α is the power-law exponent of the velocity profile.

In addition, in the book by Dyrbye et al. [21] a very similar approach is proposed, valid for heights from 10 to 200 m

$$L_u^x = 100 \left(\frac{z}{10} \right)^{0.3} \quad (2.24)$$

2.2.5 Turbulence spectrum

The turbulence spectrum describes the frequency of the wind speed variations. When the spectrum is plotted, the data must approach an asymptotic limit proportional to $n^{-5/3}$ according to Kolmogorov law in high frequencies [21]. In this limit, n is the frequency (in Hz) and the relations denotes the downgrade of the turbulent eddies to higher frequencies as the energy is dissipated as heat. Most of the kinetic energy of the turbulent motion is dissipated at the lower frequencies (where the largest eddies are), the tendency is that the turbulent eddies become smaller and smaller and exchanging less and less energy, giving name to the “energy cascade”.

The “energy cascade” phenomenon describes the development of the vortexes from the large structures they form in the beginning to the smaller structures due to the exchange of energy. This process continues, creating smaller and smaller structures which produces a hierarchy of eddies until all the energy content in the turbulent flow is dissipated.

Power spectral densities are used in dynamic analyses; furthermore the so-called power spectral density function is used when there are no turbulence power spectral densities available for a site.

As it is mentioned before, speed fluctuations in the flow make it turbulent. Wind velocity fluctuations are expressed as a composite of sinusoidal variations of wind velocities, as it were ordinary periodic waves. Due to the fact that the average value of the fluctuations is zero, they must be expressed as the square value of them. In conclusion wind speed fluctuations are expressed as the square value over the frequency forming the spectrum. From the theory it is expected a high power over the lowest frequencies decaying while increasing the frequency approximately to the asymptotic limit proposed by Kolmogorov [7,21,32].

There are several power spectrum density functions proposed based on empirical results.

Kaimal spectral density, expression proposed by Kaimal in 1972 is used by several authors in several articles and books [2,7,19,21,35].

$$\frac{nS(n)}{\sigma_u^2} = \frac{100f_z}{3(1+50f_z)^{5/3}} \quad (2.25)$$

$$f_z = \frac{n(z-d)}{U} \quad (2.26)$$

Where n is the frequency in Hertz, $S(n)$ is the power spectrum for the longitudinal component of turbulence and f_z is the reduced frequency (also known as the Monin similarity coordinate [21]), in this way it is turned into a non dimensional parameter using the height ($z-d$) and the local mean velocity $U(z)$. The height z close to the ground can be used as the turbulent length scale [21].

At low heights, up to 50m the integral length scales are proportional to the height z , for higher z , this should be replaced with f_L in the spectral density function [21].

$$f_L = \frac{nL_u^x(z)}{U(z)} \quad (2.27)$$

The Kaimal expression for spectral density gives a good approximation; it has a broader peak than Von Karman. This is practical when later the length scales are calculated using the peak frequency, with the f_z form in the expression which is not dependent of the length scales.

The Von Karman expression for spectral density is widely used as a spectral model [2,4,7,19,21,29,30,32]. It is mentioned in the book by Burton et al. [7] that recently it has been suggested that the Von Karman spectrum gives good approximation for above 150 m from the ground but is defective at lower altitudes. It gives good results with wind tunnel data too. Also in the same book it is noted that the following relation must be taken into account $L_{1u}=2.329L_{2u}$ to have the same asymptotic limit for both spectrums. Where L_{1u} is the integral length scale of Kaimal expression and L_{2u} is of Von Karman.

$$\frac{nS(n)}{\sigma_u^2} = \frac{4f_L}{(1+70.8f_L^2)^{5/6}} \quad (2.28)$$

In the Eurocode1 there is also an expression proposed to characterize the power spectrum.

$$\frac{nS(n)}{\sigma_u^2} = \frac{6.8f_L}{(1+10.2f_L)^{5/3}} \quad (2.29)$$

Which is, also mentioned in the book by Dyrbye et al. [21], more related to construction than to wind energy or fluid characteristics. However the expression is used in a scientific purpose article by Balendra et al. [2]

After doing the spectra analysis and the comparison with the expressions proposed, the integral length scales are left as the fitting parameter [16]. Some authors use the peak frequency from the expression by Kaimal to calculate the integral length scales which later are able to check with the integral dependent expressions of the spectrum, trying to match the Von Karman expression's peak to the spectral peak. They actually use two different expressions for this; the first of them is proposed by ESDU and the second is by Ficht and McVehil, mentioned later by Counihan in his review [2,19,30].

$$L_{x,u}^{(1)} = \frac{0.146U(z)}{f_M} \quad (2.30)$$

$$L_{x,u}^{(2)} = \frac{U(z)}{2\pi f_M} \quad (2.31)$$

Where f_M is the peak frequency in Hz and $U(z)$ is the local mean velocity.

These expressions are not the definitive value for integral length scales; at last it is the value which best fits the power spectra data to the proposed curves. So the determination of the integral length scales can be approached by guessing the right values of it and checking when the peak of the empirical expression for power spectral density matches with the spectral peak.

CHAPTER 3

3 Wall bounded flow

In a turbulent wall bounded flow is the vertical mixing increased compared to a laminar flow. Because of the increased mixing, the turbulent boundary layers have a higher velocity gradient near the wall than the laminar boundary layers. Turbulent boundary layers have the highest velocity gradient in the region $y/\delta < 2$.

It is common to divide the turbulent velocity profile into three main regions, inner layer, outer layer and the overlap layer [40].

- **In the inner layer** is the velocity small, and the viscous forces are dominant. Because the viscous forces are dominant, is the region also called the viscous sublayer. This layer extends often less than 2 percent of the profile [41].
- **In the overlap layer** is the profile dominated of both viscous forces and turbulent stresses.
- The region is also often called the logarithmic layer, because the velocity in this region varies logarithmically with the distance from the wall.
- **In the outer layer** is the flow totally dominated by turbulent stresses, and the velocities are not very different from the free stream velocities.

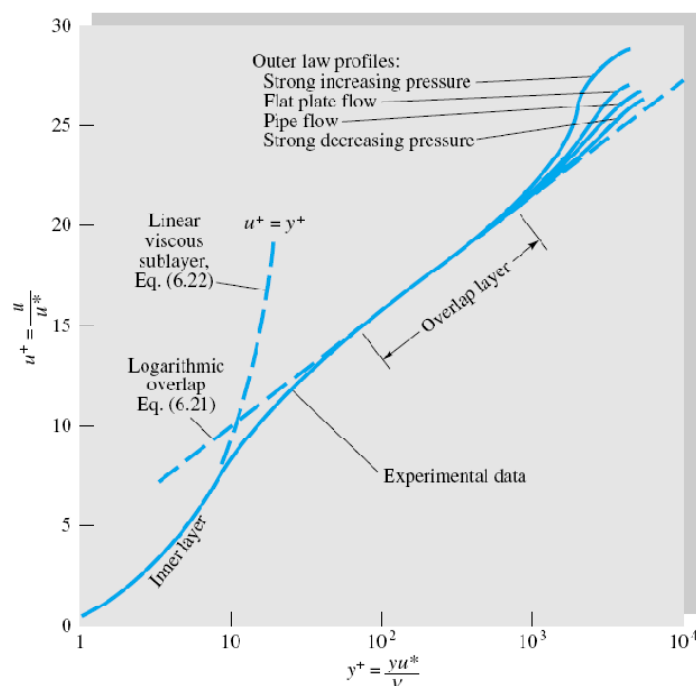


Figure 4: Verification of the different layers. Figure taken from *Fluid mechanics* book [40]

CHAPTER 4

4 Potential Flow

Potential flow is a form to characterize the fluid motion, based on the differential equations that govern its particles movement. It is an analysis that needs to fulfil the four basic conservation laws; mass, linear momentum, moment of momentum and energy to be applied to either an infinitesimal control volume or infinitesimal fluid system. In this way the differential equations of fluid motion are obtained, however as in every problem where differential equations are involved, appropriate boundary layer conditions are needed for reaching a solution [41]

4.1 Flow around a cylinder

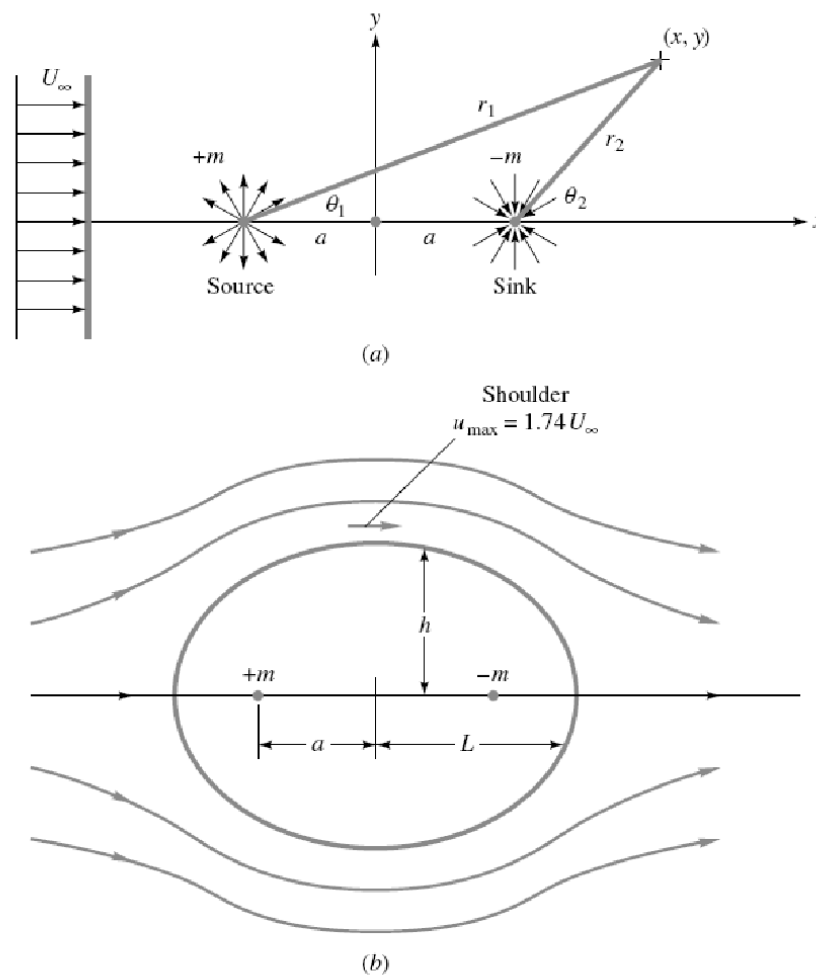


Figure 5: a) Source and sink locations. b) flow streamlines. Figure taken from *Fluid Mechanics* book [41].

The Rankine oval is a shape that is formed by a source and a sink. This form lies with its longitudinal axis parallel to a uniform stream; the source and the sink are placed along the longitudinal axis of the oval [41]. The equation describing the form is the following

$$\psi = U_{\infty}y - m \arctan\left(\frac{2ay}{x^2 + y^2 - a^2}\right) \quad (4.1)$$

The dimensions of the oval depend completely on the strength of the source and the sink. In this type of analysis the function's streamlines are plotted and an oval shape of semi-height h and semi-length L is described enclosing both source and sink. There are two pairs of points that deserve special attention; stagnation points $x=\pm L, y=0$ and maximum-velocity/minimum-pressure points $x=0, y=\pm h$ [41].

With this function the streamlines of the flow can be represented, each equipotential line is a streamline; also it can be possible to determine the velocity field by deriving the expression.

$$\begin{aligned} u &= \frac{\partial \psi}{\partial y} \\ v &= \frac{\partial \psi}{\partial x} \end{aligned} \quad (4.2)$$

The particular solution of this equation when the shape is a cylinder

$$\psi(r, \theta) = U_{\infty} \sin(\theta) \left(r - \frac{a^2}{r} \right) - K \ln\left(\frac{r}{a}\right) \quad (4.3)$$

Where U_{∞} is the flat-profile free stream velocity (boundary condition), a is the cylinder radius and K is a constant which controls the circulation of the flow. The function Ψ equals to zero on the border or the shape.

For the code used to simulate the flow in this project slight changes were made, a change of coordinates from polar to rectangular and K was set to zero.

$$\begin{aligned} r^2 &= x^2 + y^2 \\ \tan(\theta) &= \frac{y}{x} \\ \psi(x, y) &= U_{\infty} \sin\left(\arctan\left(\frac{y}{x}\right)\right) \left(\sqrt{x^2 + y^2} - \frac{a^2}{\sqrt{x^2 + y^2}} \right) \end{aligned} \quad (4.4)$$

Finally the formula for the simulation (note that y direction has been changed by z for an easier referencing in the wind tunnel)

$$\psi(x, z) = U_{\infty} \sin\left(\arctan\left(\frac{z}{x}\right)\right) \left(\sqrt{x^2 + z^2} - \frac{a^2}{\sqrt{x^2 + z^2}} \right) \quad (4.5)$$

The speed component over the cylinder is purely horizontal, so the vertical component of the velocity is equal to zero, at $(r, \pi/2)$ in polar or $(0, y)$ in rectangular. The velocity components

$$\begin{aligned} v_r &= \frac{1}{r} \frac{\partial \psi}{\partial \theta} = U_\infty \cos \theta \left(1 - \frac{a^2}{r^2} \right) \\ v_\theta &= -\frac{\partial \psi}{\partial r} = -U_\infty \sin \theta \left(1 + \frac{a^2}{r^2} \right) + \frac{K}{r} \end{aligned} \quad (4.6)$$

At the centre of the cylinder, $\theta = \pi/2$ the component $v_r = 0$, so the longitudinal velocity component is the total velocity, and the following statement can be done for the velocity profile over the cylinder $U = v_\theta$

$$\begin{aligned} U(r, \frac{\pi}{2}) &= -U_\infty \left(1 + \frac{a^2}{r^2} \right) + \frac{K}{r} \\ U(0, z) &= -U_\infty \left(1 + \frac{a^2}{y^2} \right) + \frac{K}{r} \end{aligned} \quad (4.7)$$

The minus sign of the velocity responds to axis relative locations, but without any confusion the expected velocity component must be positive in this case.

4.2 Panel method

To simulate the flow over a ramp the method described in the book by Bertin [3] was used. In a brief, the method consists of locating sources of different strength according to the shape that is wanted to achieve, the shape is represented by short segments, which can be adapted with different accuracy to any non-polygonal shape.

CHAPTER 5

5 The Norwegian Standard NS 3491-4

There are several standards developed, such as Eurocode1, Danish Standard and Norwegian Standard to help engineers to comply with the essential requirements in engineering work. One example is the Norwegian Standard (NS 3491-4), which is for example used for engineering purposes when the wind behaviour over hills and escarpment is of interest. The Norwegian Standard has empirical equations which estimate the horizontal velocity profile and turbulence intensity for different topography. The Norwegian Standard (NS 3491-4) [34] is based on the ENV 1991 1-2-4 Eurocode1- Basis of design and actions in structures-Part 2-4: Actions on structures-Wind actions. Some parts are also based on the International Standard ISO 4354:1997 Wind actions in structures and Danish Standard DS 410:1998.

5.1 Equations of Norwegian Standard

The Norwegian Standard boundary layer equation:

$$V_s = c_r(z)c_t(z)v_{ref} \quad (5.1)$$

Where:

- v_{ref} is the reference wind velocity at 10 meters above the surface.
- $c_t(z)$ is the topography factor
- $c_r(z)$ is the surface roughness factor.
- z is the height above the ground.

The surface roughness factor:

$$c_r(z) = \begin{cases} k_T \ln(z/z_0); & \text{for } z_{\min} \leq z \leq 200m \\ c_r; & \text{for } z < z_{\min} \end{cases} \quad (5.2)$$

Equation for the topography factor:

$$c_t(z) = 1 + \Delta s_{z,maks} \cdot \left[\frac{B/L_0}{B/L_0 + 0,4} \right] \cdot \left[1 - \frac{x}{k_{vir} L_H} \right] \cdot e^{-\left(\frac{az}{L_H}\right)} \quad (5.3)$$

Turbulence intensity:

$$I_u(z) = \begin{cases} \frac{c_u}{c_t(z)} \cdot \frac{1}{\ln(c_r(z)/c_t(z))} = \frac{c_u \cdot k_T}{c_r(z) \cdot c_t(z)}; & \text{for } z \geq z_{\min} \\ I_u(z_{\min}); & \text{for } z < z_{\min} \end{cases} \quad (5.4)$$

Where:

Z is the local height above the ground

L_0 is the vertical upstream distance between highest hill/escarpment top (H) and 0.5H

L_H is the vertical upstream distance between the local hill/escarpment top and the 0.5H

B is the vertical distance (orthogonal on the wind direction) between the highest hill/escarpment top to 0.5 H

a is given in table

K_{virik} is given in table

k_T is the surface roughness constant(dependent of the terrain)

$\Delta S_{z,\text{maks}}$ is given in table

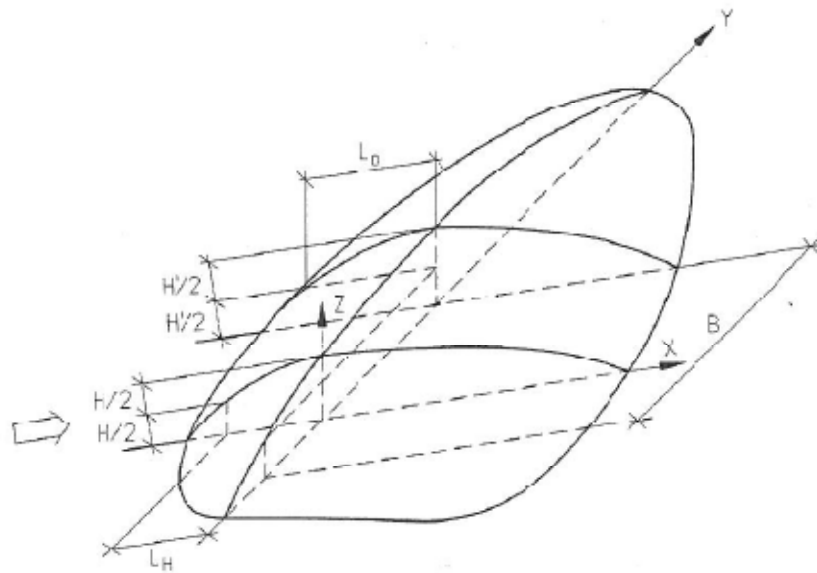


Figure 6: Hill/escarpment

Type of topography	$\Delta S_{z,\text{max}}$	a	K_{virik} for $x < 0$	K_{virik} for $x > 0$
Hill	$2H/L_H$	3	1.5	1.5
Escarpment	$1.8H/L_H$	2.5	1.5	4

Table 4: Constants used in the Norwegian Standard

CHAPTER 6

6 Simulations in a wind tunnel

To investigate wind effects on buildings, structures and transport of air pollutions in the ABL, it became necessary to develop methods to carry out realistic simulations of the ABL in wind tunnels [9-13].

One method is to let the boundary layer grow natural over a long fetch of surface roughness. The problem with the method of “natural” grown boundary layer is the required fetch of surface roughness in the wind tunnel to achieve a boundary layer with sufficient depth.

For example the 25 meters long Boundary Layer Wind Tunnel at University of Western Ontario only obtained natural grown boundary layer depths of 900mm over a fetch of simulated urban roughness and 380mm over a fetch of simulated rural terrain.

In the late 60’s and early 70’s the laboratory requirements to simulate ABL were not affordable, by then it was thought that it was needed a 27 m long wind tunnel to simulate it [9-11].

To solve the problem of long fetch requirement, has it been developed several techniques which accelerate the boundary layer growth. The methods can be divided into two main groups, passive and active methods. In this paper the focus is on the passive or also known as roughness, barrier and mixing –device methods. There are three main methods in using this type of devices, the method by Cook, the method by Standen and the method by Counihan. The different methods perform substantially the same role, but the design of the barrier and mixing-device hardware differs considerably, but the design of the roughness elements is the same.

6.1 Similarity criteria for ABL simulating in a wind tunnel

To achieve a correct dynamic and thermal simulation of the atmospheric boundary layer [12] in the wind tunnel, it must fulfill some similarity criteria. The similarity requirements for the atmospheric and wind-tunnel boundary layers can be obtained from the fundamental equations of conservation of mass, momentum and energy. (“0” is scaled by appropriate reference quantities)

- Rossby number: defines the ratio of advective acceleration to Coriolis acceleration.

$$Ro = U_0 / (L_0 \Omega_0)$$

- Gross Richardson number: represents the inertial forces to gravitational forces.

$$Ri = [(\Delta T)_0 / T_0] (L_0 / U_0^2) g_0$$

- Reynolds number: represents the ratio of inertial forces to viscous forces.

$$Re = U_\infty H / \nu$$

- Prandtl number: ratio of heat dissipation to heat conduction.

$$Pr = \nu_0 / (k_0 / \rho_0 C_{p0})$$

- Eckert number: defines the ratio of kinetic energy to enthalpy.

$$Ec = U_0^2 / [C_{p0} (\Delta T)_0]$$

For the simulation of a neutral atmospheric boundary layer in a wind tunnel the Prandtl number is equal when air is the fluid. The Eckert number is of no importance until the air velocity is close to the speed of sound. The Gross Richardson number is zero for a neutral atmospheric boundary layer.

The Rossby number limits the simulation of the atmospheric boundary layer to atmospheric flow not affected appreciably by the rotation of Earth [11]. Cermak et. al. [13] points out that if the prototype lengths are less than 100 km, the Coriolis forces do not produce large differences in flow patterns between model and the prototype.

To be sure of Reynolds number independency, the simulated boundary layer flow must be aerodynamically rough. Snyder [36] wrote that it is commonly thought that for maintenance of fully turbulent conditions the roughness Reynolds number ($Re_R = u^* z_0 / \nu$) should exceed a critical value of at least 2, although various alternative (usually higher) figures are given in the literature. Snyder observed a critical value $Re_R = 0.5$. Kozmar [30] required a $Re_R > 5$ while J.R Garret [24] demanded a $Re_R > 75$ for the flow to be aerodynamically rough.

6.2 Roughness, barrier and mixing –device methods

The role of the mixing device is to create eddies or vortices which will accelerate the outward diffusion of the high intensity turbulence produced by the roughness elements on the ground level. The surface roughness represents the roughness of the full-scale ground surface. The roughness establishes a profile of Reynolds stress through the layer which in turn controls the mean velocity profile and the turbulence characteristics. The roughness is the most important component of the hardware to achieve a correct simulation of the ABL because it establishes the values of the three law of the wall parameters: surface length z_0 , displacement thickness d and friction velocity u^* .

The role of the barrier is to give the flow a momentum deficit and depth to the layer which is mixed into the layer by the turbulence generated by the mixing-device.

6.2.1 Short description of the hardware

The method by Cook [17] uses a square mesh grid as the mixing device. Further downstream of the mixing-device the barrier was placed. In the first attempts a plane wall as the barrier, but later perforations were added near the top. Counihan [18] used also a barrier and mixing device, but the barrier wall was placed upstream of the mixing device. The barrier was a castellated wall, with an increase in the local height of the wall immediately upstream of the mixing device. For the mixing device Counihan used a row of elliptic wedge vorticity generators [18]. Standen [25] developed a method to accelerate the boundary layer growth by using only a row of spires instead of a separate barrier and mixing device. The empirical design rules for the Standen spires, was developed by Irwin [25].

Nowadays the method by Standen and Counihan is still widely used for simulations of the ABL in wind tunnels. Simulations with the Standen spires results in a boundary layer thickness about 20% smaller than the spire height, and for the method by Counihan the boundary layer depth becomes approximately of the same height as the elliptic wedge vorticity generators [22,28]. During the research for this project articles that used the three methods were found, articles using the Counihan method [2,4,22,28,2930,] articles using the Standen method [4,31,38] and articles using Cook's [16,17].

6.2.2 Full depth and part depth simulations

When the ABL flow through the whole depth is reproduced in a wind tunnel, it is called full-depth simulations [2,28,29,31,38]. The problem with full-depth simulations is the scale ratio. A typical scale ratio for a full-depth simulation is in the range 1/200 - 1/1000. To achieve a smaller scale ratio, (for example 1/100) it is impossible to simulate the entire depth of the total atmospheric boundary layer due to the facilities needed to achieve that would be unaffordable. Instead of that a simulation of the lower part of the atmospheric boundary layer can be done, and is called part-depth simulation. It is possible to do this type of simulations using either modified Standen or Counihan methods as it is indicated in the article by Bortoli et al. [4,30], or Cook method, specially designed to simulate the lower third of the ABL [15,17]. The modified Standen and Counihan methods consist in truncating the spires at a determined height of interest.

6.3 Determination of the key parameters

There are three different approaches to determinate the key parameters roughness length, friction velocity and displacement thickness for the boundary layer [16].

The error-in-origin method determines the three parameters by fitting the measured mean velocity profile near the wall to the logarithmic law-of-the-wall and is the method used in this project.

Another approach is to do an independent estimate of the friction velocity, by either surface stress measurement $u_* = (\tau_0/\rho)^{1/2}$ or measurement of the maximum Reynolds stress $u_* = (-\overline{uw})^{1/2}$.

The two remaining parameters, (roughness length and displacement thickness) are estimated by fitting the measured mean velocity profile near the wall to the logarithmic law-of-the-wall. Cook [16] showed that the approach with an independent estimate of the friction velocity, gives a much smaller variation than the error-in-origin method.

6.4 Determination of the model scale-factor of the simulated ABL

6.4.1 Jensen's number/model law

In 1958 Martin Jensen [21] formulated the condition for a realistic model tests: *"The flow in the wind tunnel should be turbulent in the same way as the flow in the natural wind"*

Jensen's model law demands that the ratio between the height of the structure/boundary layer thickness and the roughness length of the surrounding terrain is equal for the wind tunnel simulation and the atmospheric boundary layer.

Jensen model law (M is for model and F is for full scale):

$$\left(\frac{h}{z_0}\right)_F = \left(\frac{h}{z_0}\right)_M \quad \text{or} \quad \left(\frac{\delta}{z_0}\right)_F = \left(\frac{\delta}{z_0}\right)_M \quad (6.1)$$

When Jensen's model law is satisfied, the turbulence vortex structures and hence the spectra of the natural wind will be simulated with reasonable accuracy in the wind tunnel.

Jensen also introduced the similarity criteria as a non-dimensional number, named the Jensen Number:

$$Je = h / z_0 \quad (6.2)$$

The drawback with the Jensen scale-factor method is the dependency of the boundary layer thickness. For part-depth simulations, the boundary layer thickness is unknown.

6.4.2 The method developed by Cook

N.J Cook developed a standard method a method to calculate the scale-factor using the roughness length and the longitudinal integral length (u-component) of the turbulence [16]. This method checks from the bottom to the top that the fluctuating parameters of the simulation are linearly scaled with the atmospheric data. The method estimates the scale-factor independently of the boundary layer thickness, so the method is valid for both full and part-depth simulations and it is used in several articles [2,4,29,30].

Cook describes two different approaches to estimate the scale-factor, the graphical iteration method and the direct method.

6.4.2.1 Graphical iteration method:

The graphical iteration method suggested by Cook uses measurements or an empirical equation for full scale L_u^x to determine the scale-factor S by iteration.

The approach begins with assuming an initial scale-factor S_0 , to calculate the full scale surface roughness and displacement thickness.

$$z_{0F} = S_0 \cdot z_{0M} \quad (6.3)$$

$$(z-d)_F = S_0 (z-d)_M \quad (6.4)$$

In the article by Cook, it is used the empirical ESDU equation to estimate the full scale and model L_u^x .

$$L_u^x = 25(z-d)^{0.35} z_0^{-0.063} \quad (6.5)$$

But the author mentions the possibility to use any other source of data for L_u^x . In this project the empirical formula proposed by Walshe [2] is used.

The final step of the iteration is to estimate the new scale-factor. The new scale-factor is estimated as the ratio between the full scale and the model L_u^x .

$$S_{new} = \frac{(L_u^x)_F}{(L_u^x)_M} \quad (6.6)$$

The iteration process is repeated until the new scale-factor and the old one become the same.

6.4.2.2 Direct approach

In the direct approach method the scale-factor is estimated from a scale-factor equation, developed from the ESDU empirical equation for L_u^x .

Each full-scale parameter in the empirical ESDU equation is replaced by the product of the scale-factor and model parameters. From this a solution for the scale-factor S is obtained.

$$S = \frac{91.3(z-d)_M^{0.491}}{L_{uM}^{1.403} z_{0M}^{0.088}} \quad (6.7)$$

Since the L_u^x is dependent of the height above the surface, the scale-factor must be calculated at a range of different heights in the model boundary layer. The final scale-factor is the average of the different scale-factors.

There are important parameters that should be checked when scaling up the simulated boundary layer, however it is very difficult to fit all the parameters. The most important parameters that should have a similar value to the real parameters after scaling them up are: longitudinal integral lengths, roughness length, longitudinal turbulence intensity and longitudinal power spectral densities. It is also recommendable that the following parameters should fit: turbulence intensities and power spectral densities of the lateral and vertical velocity components.

6.4.3 The approach by Balendra

Balendra [2] concluded that it is almost impossible to simulate the atmospheric boundary layer with exact similarity. Balendra suggested an approach where the most important flow parameters are compared between the experiment and full scale atmospheric data, which was acceptable for wind engineering applications.

The scale method begins with a preliminary estimation of the scale-factor based on the ratio between the boundary layer thickness of the full scale atmospheric data and the experiment.

After the first estimation of the scale-factor, five of the flow parameters from the experiment are scaled up, and compared with the full scale atmospheric data.

The five flow parameters are:

- Surface roughness length.
- The vertical mean velocity profile.
- The longitudinal turbulence intensity.
- The power spectrum of longitudinal velocity fluctuations.
- The integral length scales of longitudinal velocity fluctuations.

Finally the scale-factor is adjusted until it gives a good average fit between the flow parameters in the experiment and the full scale data.

CHAPTER 7

7 Experimental set up

Due to the dimensions of the wind tunnel ($0.5 \times 1 \text{ m}^2$ section and 7m length) it was chosen to do a part-depth simulation, which would give a higher scaling factor. In the same way it was chosen the method by Counihan [19] to accelerate the growth of the boundary layer and because the quarter elliptic spires give the possibility for the layer to grow up to the top of them, not as the Standen spires which allow 80% height of spires.

As seen in the articles by Kozmar the total height of the boundary layer would be achieved at the top of the spires, so as it is intended a boundary layer of 0.5 m, 0.5m spires are needed the same as the working height permits. The decision of truncating the spires at 80% of them will be explained in section 7.2.

Here is a sketch of the final arrangement inside the wind tunnel

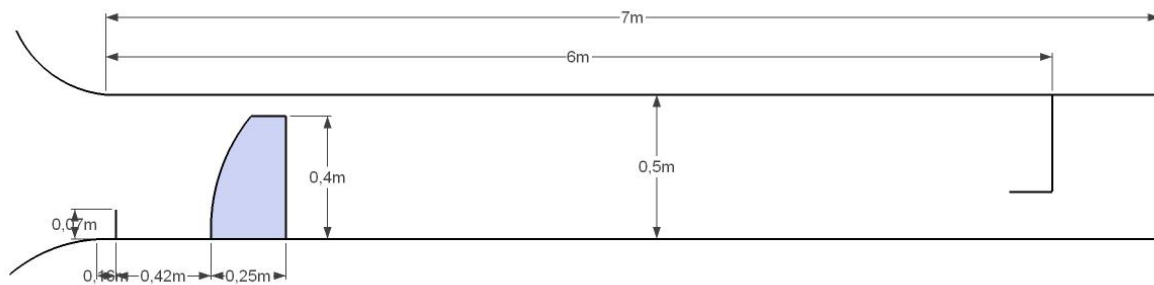


Figure 7: Wind tunnel arrangement sketch.

In order of arrangement, the barrier with a separation of one third of the boundary layer height from the tunnel contraction is located in the first position. The height of the barrier affects the turbulence directly, as a higher barrier creates more turbulence. After that it is left a blank space downwind of the barrier up to the spires which should not be less than five-sixths of the boundary layer height. Downwind of the spires, the distance between the end of the spires and the starting point of the roughness elements was not found to be important, but in this project, that distance was chosen to be zero because of the importance of the longer fetch the better.

7.1 Castellated barrier wall

The castellated barrier wall was made by scaling down the designs described in some articles [2,28,30]. Two different heights were used, 73 mm and 93mm. It was found that the lower barrier gave a smoother profile, and also a slightly higher power-law exponent than the high one, which obeys that a higher barrier creates more turbulence.

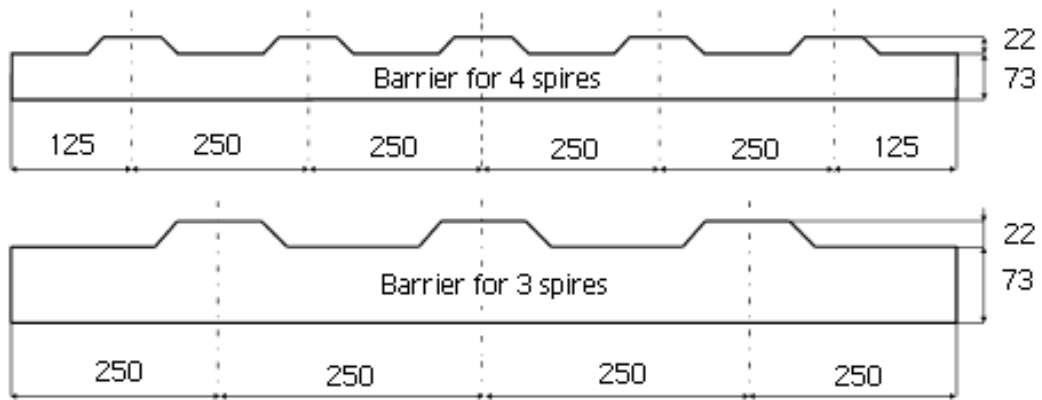


Figure 8: Dimensions of the barriers.

Surprisingly, the blank space between the barrier and spires was found to be very important; this is because in early configurations this length was set by error to one-fifth of the boundary layer height, which led to strange results in profile shape.

7.2 The Spires

A number of different methods [17,18,25] can be used to simulate the atmospheric boundary layer in a wind tunnel. Since the experiment was carried out in a 0.5 m high \times 1 m wide \times 10 m long test section, was it clear that it was a need to accelerate the boundary layer growth by using a “barrier and mixing-device hardware” method. As explained before; from private corresponding with Assistant Professor Hrvoje Kozmar [28-30] (University of Zagreb) was it recommended to use spire height of 80-85% of the wind tunnel height or lower.

Because of the limited test section height of 0.5 m, it seemed reasonable to use quarter-elliptic, constant wedge-angle Counihan spires [18] since they create a boundary layer of the same thickness as the height of the spires.

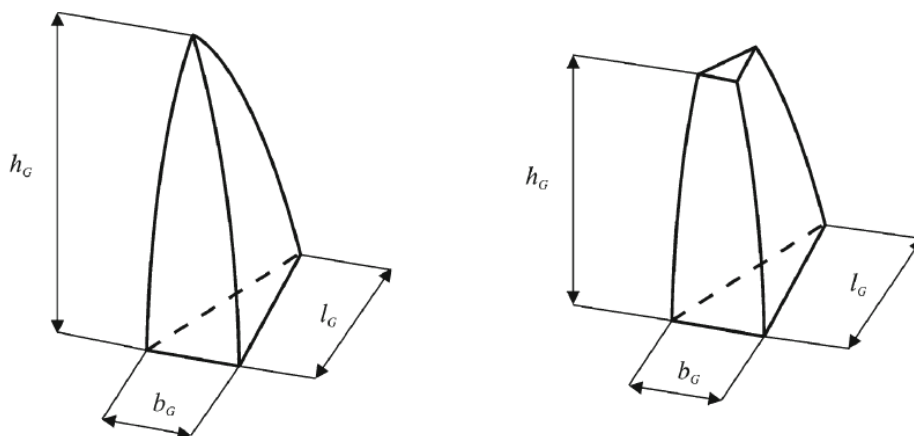


Figure 9: Quarter-elliptic, constant wedge-angle Counihan spires

For the experiment it was manufactured four spires with a height of 50 cm (h_G) and truncated to a height of 42 cm (h_G) later. The reason for using truncated spires was to obtain larger

simulation length scales. Counihan [18] experiments showed that quarter-elliptic spires with a constant wedge-angle of 6° with a spacing of 0.5-0.6 boundary layer heights, gave the best results. With a constant wedge-angle of 6° and a spire height (before truncated) of 0.5 meters, lead to a b_G and l_G of 52.5 mm and 250 mm. The spires were manufactured of steel plates which were welded together.

Two configurations were made, one with three spires and another with four spires. The spacing between spires in both configurations was half of the height of the boundary layer.

7.3 Fetch of roughness elements

For the fetch of roughness elements standard sand paper attached to thin wood plates was used. There is little or none information about using roughness elements in low power-law-exponent profiles, in other words, over smooth terrains. Bortoli et al. [4] simply used free floor or partially covered it of roughness elements and then empty floor achieving exponents of 0.09 and 0.14. Carpenter et al. [8] used textured wallpaper (average height of texture elements 1mm) to achieve a Deaves and Harris Category 2 profile [14] which corresponds to an exponent of 0.16. With this information it looks reasonable to use sand paper as roughness fetch to achieve a low power-law exponent around 0.12, corresponding a terrain category 0 by Deaves and Harris, category I by Eurocode1, between categories 2 and 3 by Davenport.

7.4 Simulation over a cylinder

Two standard PVC cylinders for piping were used for the simulations; both were cut in half over their longitudinal axis. One of them has a diameter of 5 cm and the other is 12 cm. Only with the big cylinder it was possible to achieve in clear the $Re > 9 \cdot 10^4$ region that the non-dimensional flow characteristics are independent of the Reynolds number [23].

$$Re = \frac{U_\infty H}{\nu} \quad (7.1)$$

Where H is the height of the cylinder (at half of the diameter), U_∞ is the free stream wind velocity and ν is the kinematic viscosity of the air.

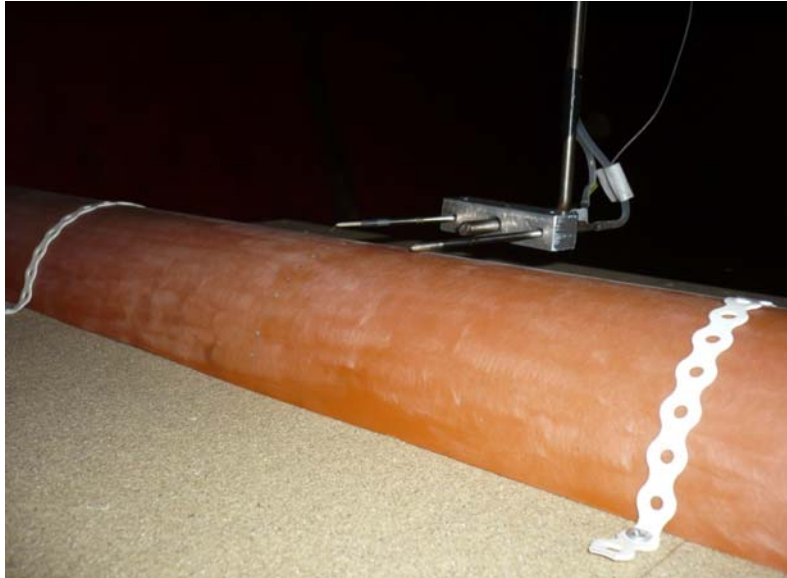


Figure 10: Half cylinder placed in the wind tunnel

7.5 Simulation over a ramp

A ramp model made of wood was manufactured to experiment with in the wind tunnel. The particularity of the ramp against the cylinder is that the separation of the flow occurs at the same point independently of the velocity of it. The separation takes place at the intersection between the inclined plane and the horizontal plane. The dimensions of it are a total height of 7 cm, a slope angle of 47° ($H=70\text{mm}$, $L=65\text{mm}$) and a horizontal plane length enough to not disturb the flow separation downwind.

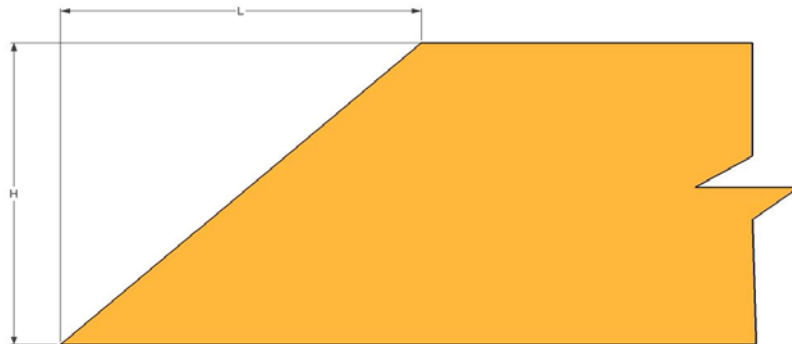


Figure 11: Ramp dimensions.

7.6 Blockage effect

When a model is attached inside a wind tunnel it can create blockage. If the model takes up a significant area relative to the cross section of the wind tunnel, the blockage will speed-up and distort the flow. A model should not block more than 10-15% of the cross-section of the wind tunnel. If the blockage ratio is less than 10-15% the flow acceleration is not expected to alter the longitude pressure gradient enough to affect the flow significantly [35].

CHAPTER 8

8 Results

8.1 Artificial growth of the ABL

To justify the use of the barrier and elliptical vortex generators to accelerate the growing of the ABL, it was done a trial with only the roughness fetch placed in the wind tunnel of an approximate total length of 5 meters.

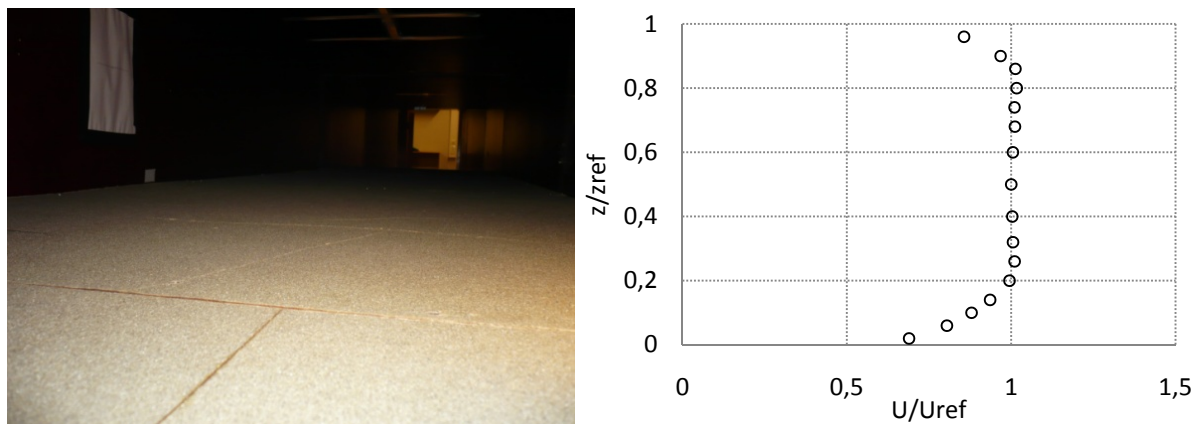


Figure 12: Picture of the 5 m of roughness fetch (left). Velocity profile of the empty wind tunnel.

This height of ABL, scarce 11 cm, is not valid for a substantial experimentation, either a longer fetch is needed or a barrier and mixing-device is needed.

8.2 Similarity



Figure 13: Barrier, spires and roughness fetch installed in the wind tunnel.

Two set ups were arranged, one with three spires and another with four spires.

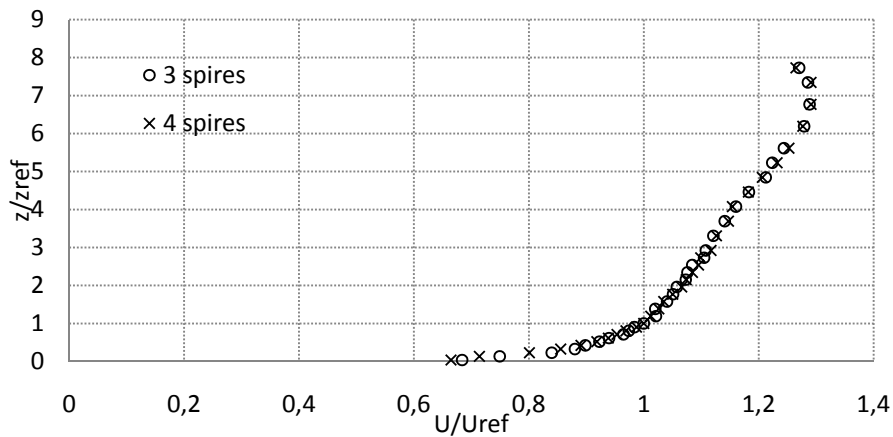


Figure 14: Velocity profile of 3 and 4 spires.

The results in both set ups were identical, and both were valid up to 380 mm. Above this height, the velocity started to decrease. 380 mm is less than the predicted 400 mm high boundary layer.

The boundary layer was also measured at different lengths of the fetch.

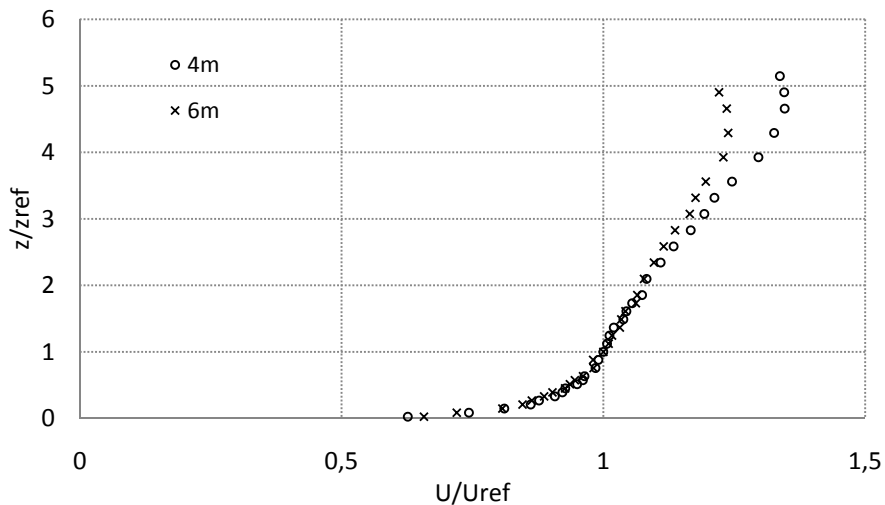


Figure 15: Velocity profile at different lengths of fetch.

The profile is smoother with longer fetch, as the boundary layer has more time to mix and homogenise itself. Also the boundary layer decreases a little (between one and two centimetres), as it can be seen the velocity starts to decrease later with 4 m fetch. The overall characteristics of the boundary layer developed 6m downwind from the wind tunnel constriction are better than the one 4m downwind.

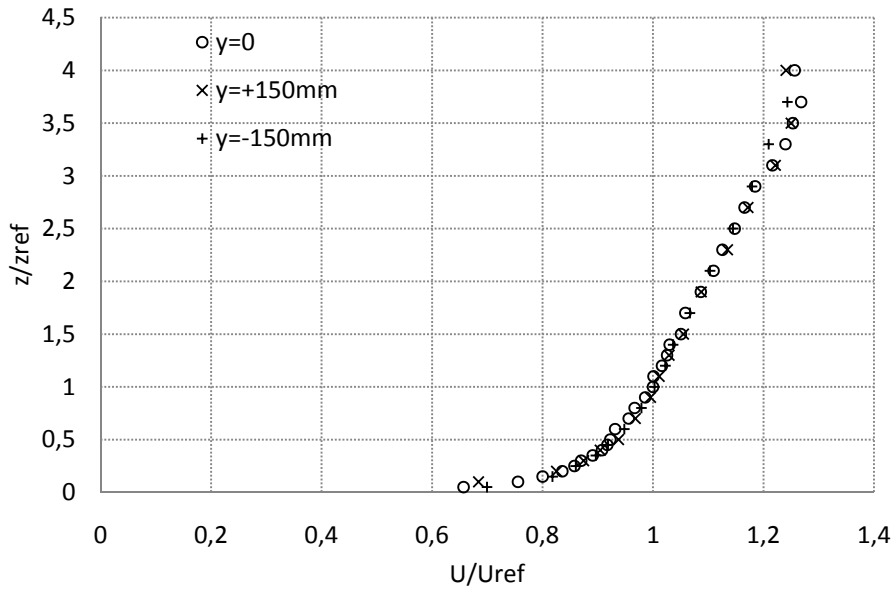


Figure 16: Velocity profile at the center and both sides.

It is represented here the boundary layer at the center of the tunnel ($y=0$), and from a distance at both sides ($y=-150\text{mm}$, $y=+150\text{mm}$) with a satisfactory result of similarity. This assures that the profile is the same in the complete working section.

The velocity profile at 6m gave a better fitting to theoretical power-law profile although it is identical to the log-law fitting because up to 150mm both profiles match in every point.

8.2.1 Power-law and log-law fitting

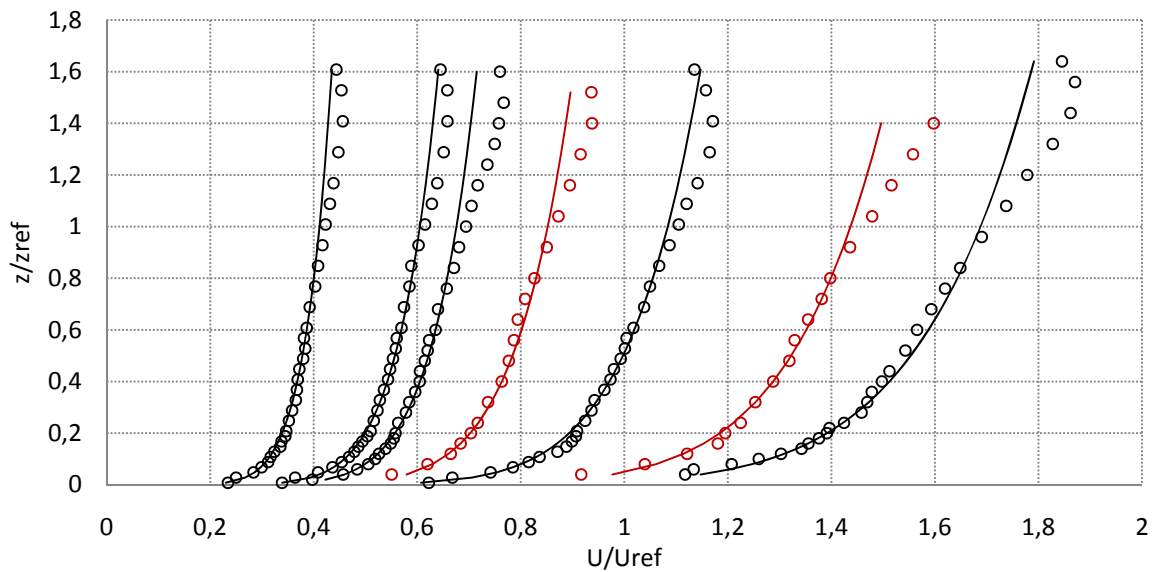


Figure 17: Velocity profile at different velocities.

There are plotted seven velocity profiles with the same arrangement of seven centimeter barrier, four spires and six meter fetch at different wind velocities against the power-law with a reference height of 100 mm and an exponent of $\alpha=0.12$ (they have been non-dimensionalized with a $z_{ref}=250\text{mm}$ and $U_{ref}=15\text{m/s}$). This plot shows the consistency of the profile that conserves acceptably the power-law profile shape over different wind speeds. The profiles in red are later used for simulating the flow over obstacles for cases 1 and 2 note that the profile for case two has an overall larger velocity. This velocity was sufficient to try to fulfil the Reynolds number independence and enough to not exceed the calibration limits.

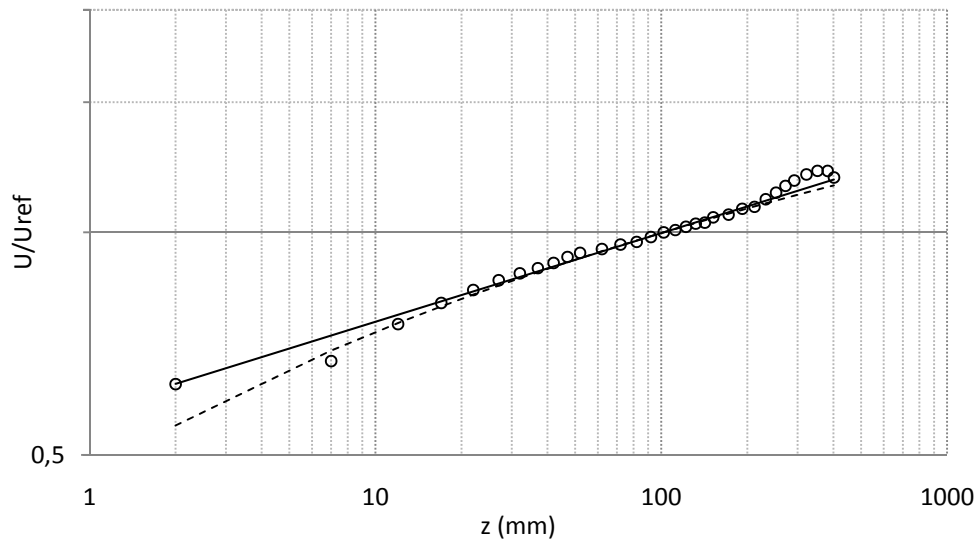


Figure 18: Log-law and power-law fitting.

A power-law fitting of $\alpha=0.12$ (solid line) and a log-law fitting of $u^*=0.43\text{m/s}$ and $z_0=0.000017\text{m}$.

8.2.2 Spectrum

The spectrum was calculated using Welch's averaged modified periodogram method of spectral estimation with a Hanning style window of 2^{14} samples length, with an overlap of fifty percent and a total number of windows of 50. The size of the windows was chosen to be the optimum, big enough to close the spectrum at low frequencies and small enough to be clear.

Spectrum of the on-set profile for the experiments with the escarpments (case 1).

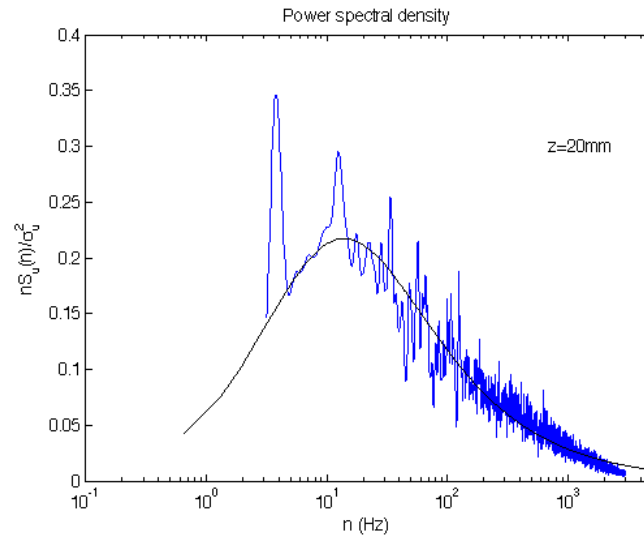


Figure 19: PSD and kaimal distribution.

Power spectral density plotted non-dimensional against the Kaimal distribution using the reduced frequency. The integral length obtained was $L_u^x=0.11m$.

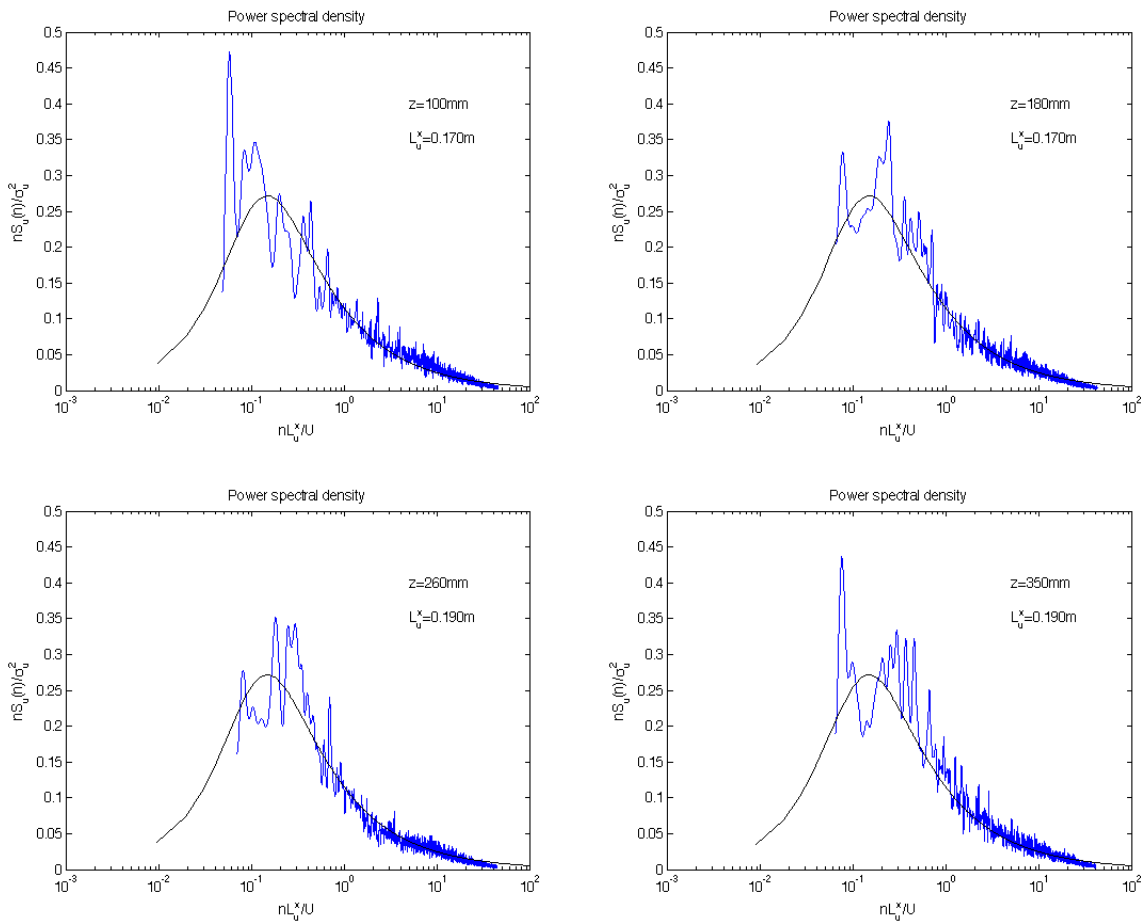


Figure 20: PSD of longitudinal velocity fluctuations at different heights and the correspondent Von Karman distribution.

Spectrum of the on-set profile for the experiments with the escarpments (case 2).

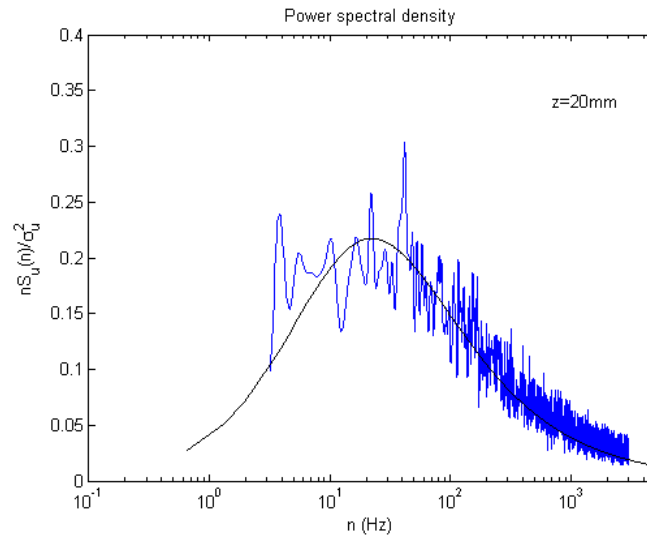


Figure 21: PSD and kaimal distribution.

Power spectral density plotted non-dimensional against the Kaimal distribution using the reduced frequency. The integral length obtained was $L_u^x=0.12m$.

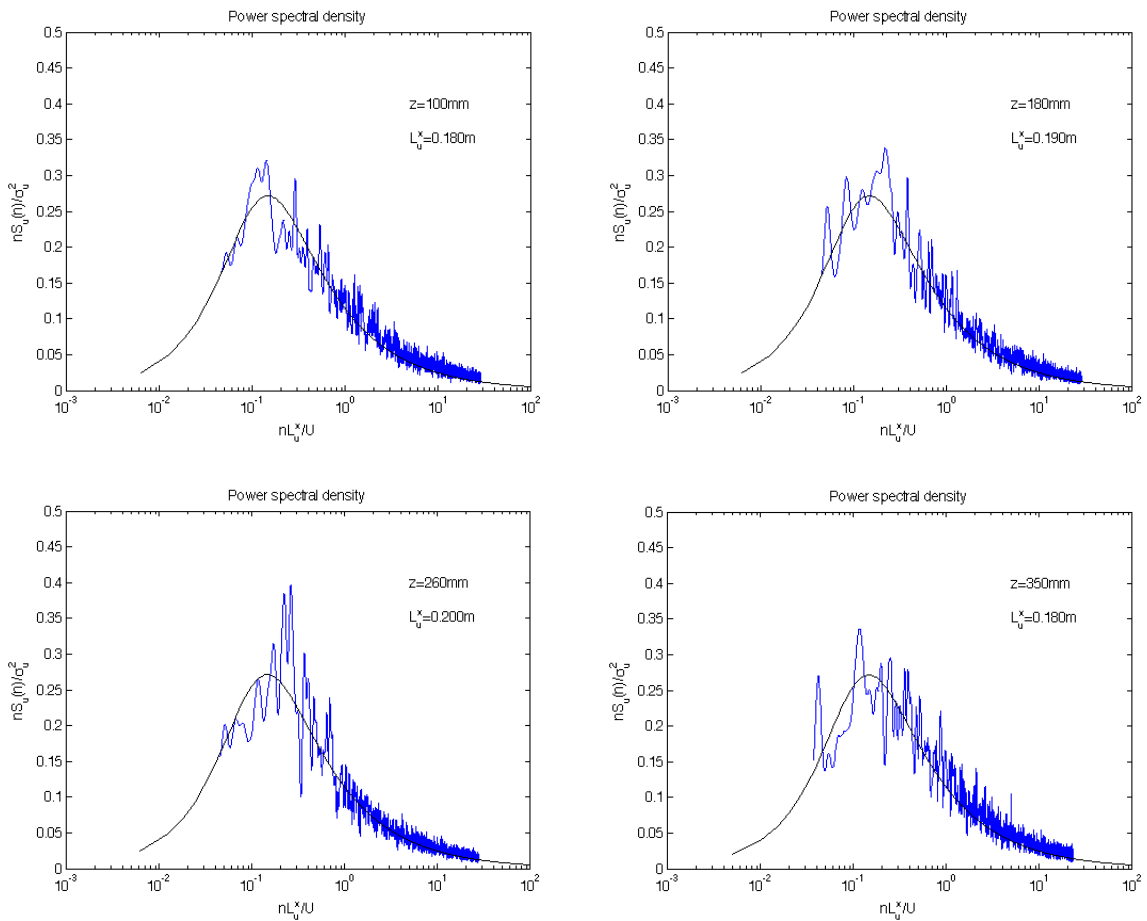


Figure 22: PSD of longitudinal velocity fluctuations at different heights and the correspondent Von Karman distribution.

Figures 19 and 21 that show power spectral densities together with Von Karman distribution at different heights, show good agreement between them and hence a right decaying of the turbulence.

8.2.3 Integral lengths

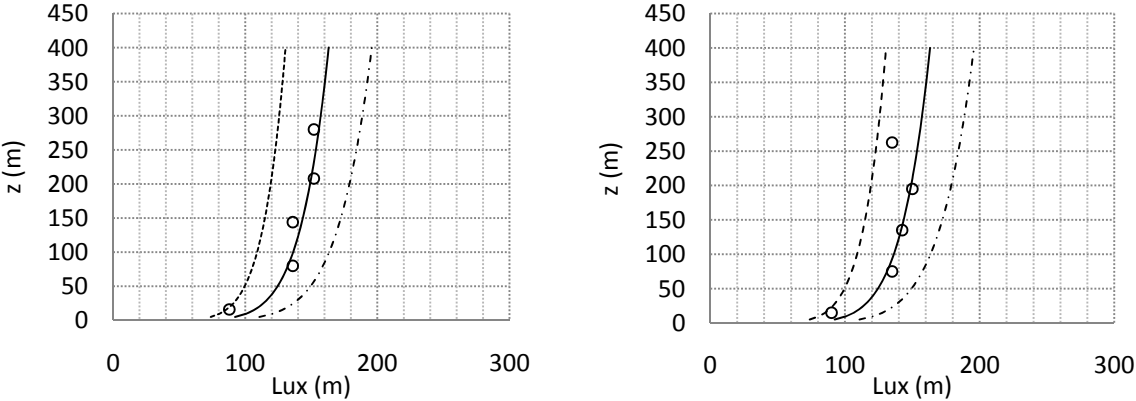


Figure 23: Integral length scales. For case 1 (right) and case 2 (left).

Integral length scales plotted against Walshe. In both cases the integral lengths obtained from the spectra were scaled up to 1:800 and 1:750, for the case 1 and case 2 respectively. Both profiles fall between a $\pm 20\%$ errors of Walshe estimation, which is acceptable in practice [2].

The graphical method by Cook was used to calculate the scale-factor, which focuses mainly on the integral length scales.

8.2.4 Roughness length

The roughness length found for the two profiles after fitting them to the logarithmic law was $z_0=1.62 \cdot 10^{-5}m$ and $z_0=2.32 \cdot 10^{-5}m$, for the case 1 and case 2 respectively. This z_0 correspond to a Terrain Category I in the Eurocode1 ($z_0=0.013m$ and $z_0=0.017m$ after scaling them up). The described Terrain Category I are “lakes or flat and horizontal area with negligible vegetation and without obstacles”.

Shear velocity was also obtained by logarithmic law fitting together with the roughness length. The values obtained were $u^*=0.535m/s$ and $u^*=0.95 m/s$, for the case 1 and case 2 respectively.

8.2.5 Roughness Reynolds number

The two profiles also satisfy the requirement of fully turbulent flow by having a larger roughness Reynolds number than 0.5 [36]. Re_R equals to 5.78 in case 1 and 1.47 in case 2.

8.2.6 Turbulence intensity

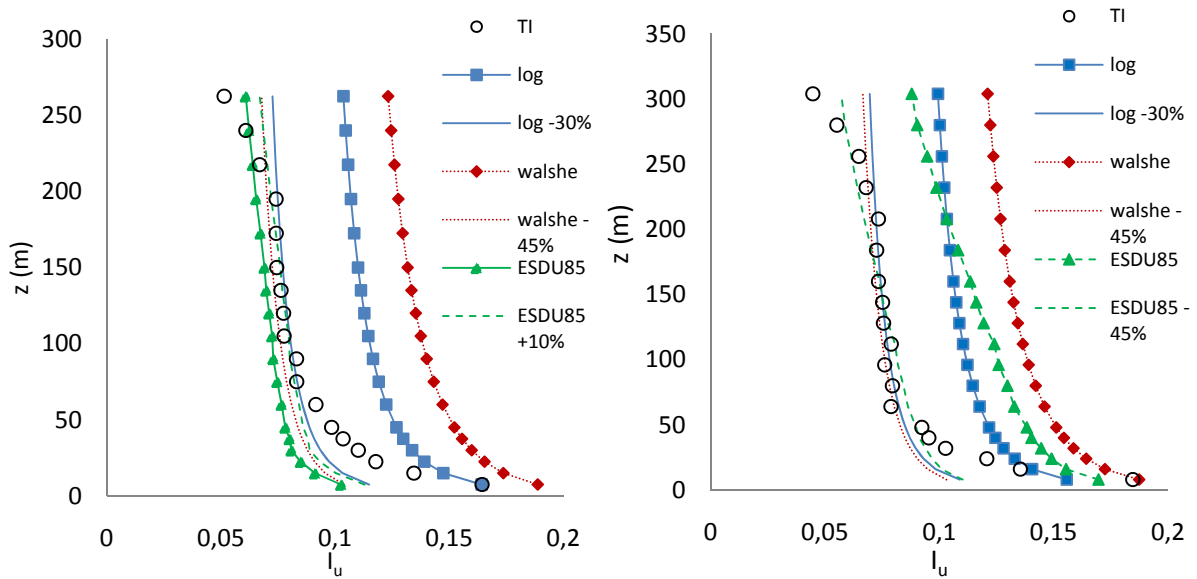


Figure 24: Turbulence intensity. For case 1 (left), for case 2 (right).

Turbulence intensity is lower than expected, although it shows the same shape. An exception must be made with the turbulence intensity of the ramps' on-set velocity profile and ESDU85 data which is slightly lower than the data from the wind tunnel. However both profiles show the tendency of $\sigma_w/U \approx 2.5$ close to the ground.

8.3 Flow over obstacles

On hills or escarpments the local velocity is higher than the surrounding area. This is because when air meets a hill/escarpment the air is compressed at the upstream side, which leads to an acceleration of the air. In this experiment the fractional speed-up and turbulence intensity is investigated for the flow above one hill peak and the very crest of an escarpment. The sharp-edge escarpment in case 1 has the dimensions $H = 0.07\text{m}$ and $L=0.065\text{m}$. The hill is modeled by a half-cylinder with a diameter of 0.125m and the results are shown in case 2. In both cases the obstacles were positioned with their longitudinal axis perpendicular to the longitudinal axis of the wind tunnel and covering all the width of its section.

8.3.1 Inflow Conditions; case 1

In case 1 the on-set profile is deeply described in section 8.1. The arrangement was made with a 73mm barrier, 4 truncated Counihan type spires and a 5 m sandpaper roughness fetch. The model was set 6 m downwind the tunnel constriction. This arrangement corresponds to a 1:800 scale of a terrain category I.

To estimate the speed-up effects, the reference velocity was kept constant at $U_{\text{ref}} = 11.3813$ m/s with $Z_{\text{ref}} = 0.1\text{m}$ for the onset velocity profile. U_{ref} , Z_{ref} and the model height H , were used as reference values for the escarpment in case 1. The undisturbed upstream simulated

atmospheric boundary layer was measured, and used as a reference profile to show the speed-up effects for the mean horizontal velocity and the turbulent properties.

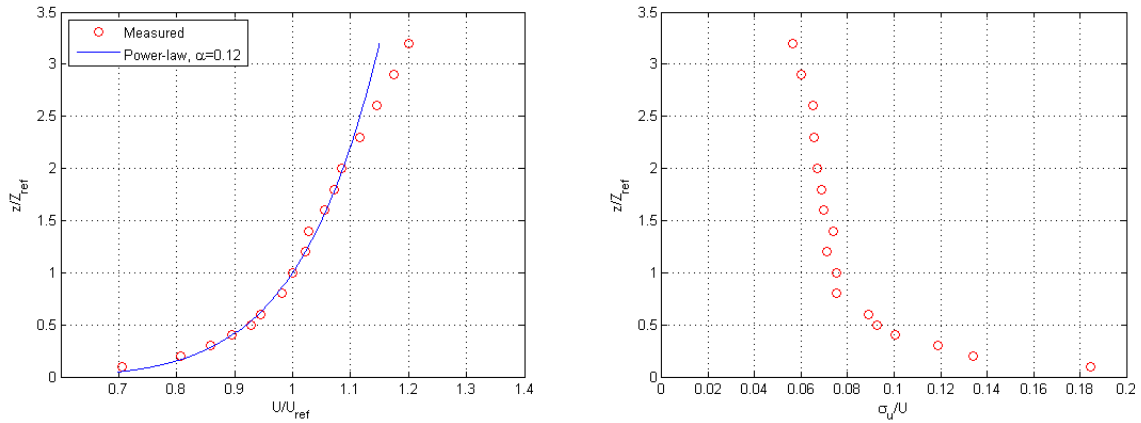


Figure 25: Velocity profile compared to the power-law (left). Turbulence intensity of the profile (right).

CASE 1

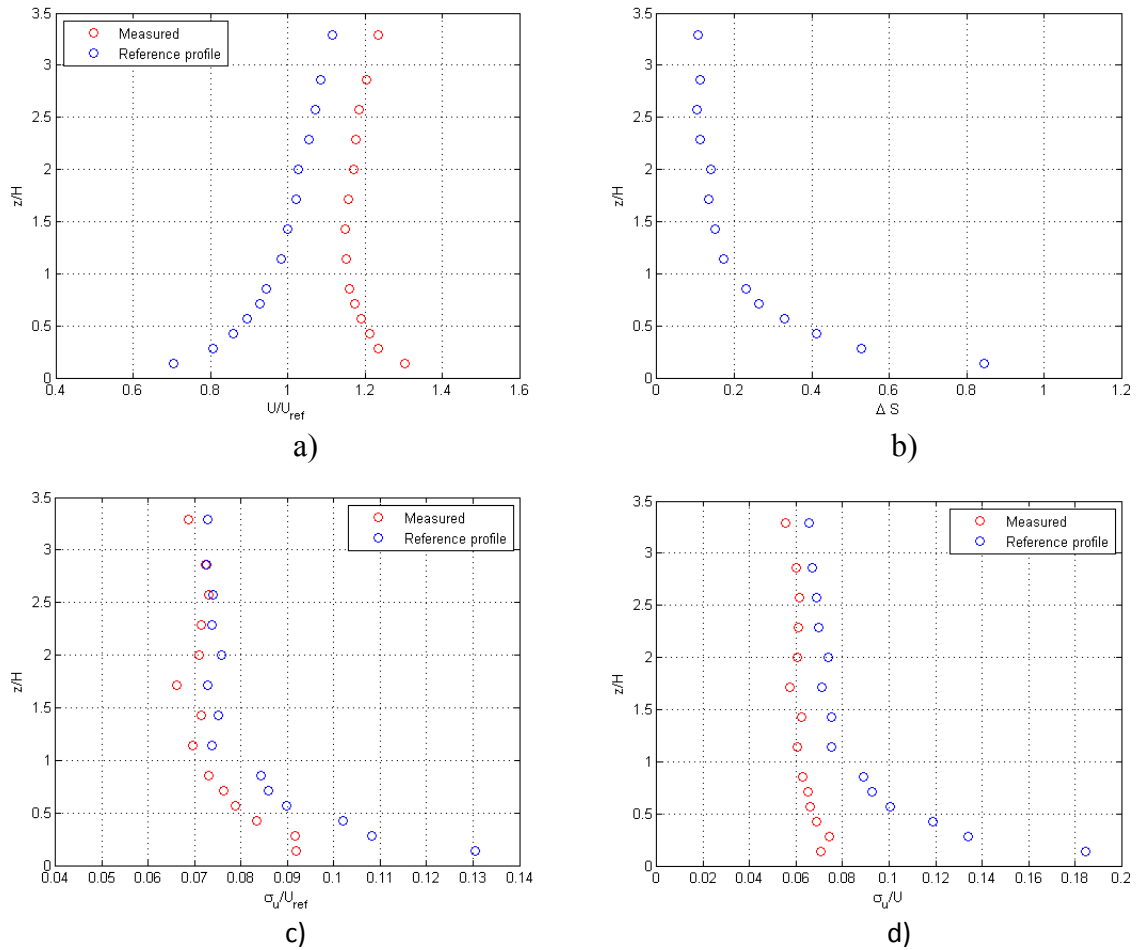


Figure 26: a) Mean horizontal velocity profile compared with the reference profile. b) Fractional speed-up (ΔS). c) The normalized standard deviation compared with the reference profile. d) Turbulence intensity compared with the reference profile.

8.3.2 Velocity and fractional speed-up

In figure 25a the measured horizontal mean velocity profile above the very crest of the escarpment is compared with the reference profile. The Figure show a considerable increase in the mean velocity near the surface. The mean horizontal velocity speed-up effects are better displayed in figure 25b which show the fractional speed-up, $\Delta S = U(z) - U_0(z) / U_0(z)$, where $U_0(z)$ is the mean horizontal velocity of the incoming flow upstream of the escarpment and $U(z)$ is the mean horizontal velocity above crest of the escarpment. A wind tunnel experiments with emphasis on wind flow over sharp-edged escarpments by A.J Bowen and D. Lindely [5], showed a fractional speed-up for the flow of between 0.7 and 0.8 at the height $z/H=0.2$ above the crests. Røknes and Krogstad [35] observed a ΔS for a sharp edged escarpment of approximately 0.6 at $z/H=0.2$ above the crest.

The measured fractional speed-up in figure 25b are 0.85 for at $z/H=0.14$. This result is in good agreement with the findings of A.J Bowen et. al [5] and Røknes et. al. [35]

The model has a blockage ratio of 14%. A very simple estimate based on the principle of continuity, results in an increase in horizontal mean velocity of 16% above the crest. This may be some of the reason for the difference between the measured velocity and reference profile in the upper part of the flow above the crest.

8.3.3 Normalized standard deviation and local turbulence intensity

In figure 25c the normalized standard deviation (σ_w / U_{ref}) for the escarpment is compared with the incoming reference profile. In case 1 the normalized standard deviation are less than the reference values between the lowest measurement point ($z/H = 1/7$) and approximately $z/H = 1.3$. Above this point, the difference between the measured normalized standard deviation and the reference values are small.

An adverse or a favourable stream-wise pressure gradient can cause large changes in an external turbulent wall flow above $y^+=50$. When the flow has a favourable pressure gradient, the turbulence statistics (u'_{rms} and v'_{rms}) decreases but causes an increase in the wall shear. The opposite will happen for a flow with an adverse pressure gradient, the turbulence level will increase and the wall shear will decrease. The adverse pressure gradient will eventually lead to a separation from the wall [40]. From the leading edge of the escarpment and to the crest of the escarpment the flow has a favourable pressure gradient and experiences a strong convective acceleration, which leads to a weak laminarization in the lowest part of the boundary layer.

In figure 25d turbulence intensity ($\sigma_w / U(z)$) is compared with the reference profile. The results show that the turbulence intensity profile at the very crest of the escarpment is considerably more uniform with height compared to the reference profile. As expected, the figures also show a decrease in the turbulence intensity compared to the reference profile. The reason for the decrease is the increase in mean velocity and the decrease of the normalized standard deviation in the lower part of the boundary layer.

CASE 2: The Hill

Flow over a two-dimensional hill was also investigated. The hill model was a wall mounted half-cylinder which was attached perpendicular to the wind direction. For this experiment the reference velocity was increased to $U_{ref} = 18.8$ m/s with a $Z_{ref} = 0.1$ m. The increased velocity was chosen in order to achieve a Reynolds number greater than the value mentioned by Ferreira.

Ferreira et al. [23] observed in their experiments that the non-dimensional flow characteristics are independent of the Reynolds number for values greater than $9 \cdot 10^4$. Ferreira used the free-stream velocity of the ABL as the U_∞ to calculate the Reynolds number. In case 2 assuming a free-stream velocity of 23.44m/s at the height of 500mm $Re=93763$, which fulfils the conditions. Stig Sund [37] found the experimental results for C_D with different Reynolds numbers for the same cylinder that was used as a hill model in our experiment. His results showed the same trend, but no exact Reynolds number limit were observed.

8.3.2 Inflow conditions; case 2: the hill

In case 2 the on-set profile is deeply described in section 8.1. The arrangement was made with a 73mm barrier, 4 truncated Counihan type spires and a 5 m sandpaper roughness fetch. The model was set 6 m downwind the tunnel constriction. This arrangement corresponds to a 1:750 scale of a terrain category I.

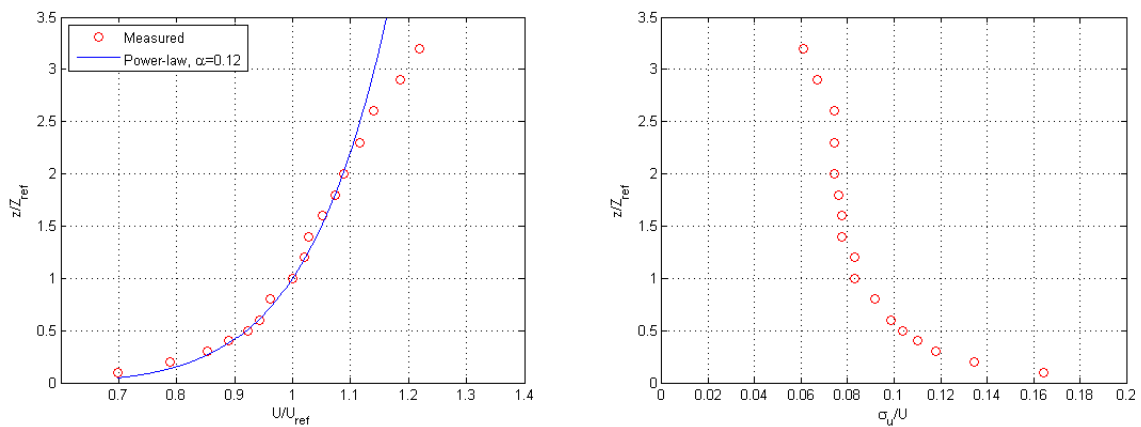


Figure 27: Velocity profile compared to the power-law (left). Turbulence intensity of the profile (right).

Case 2: the hill

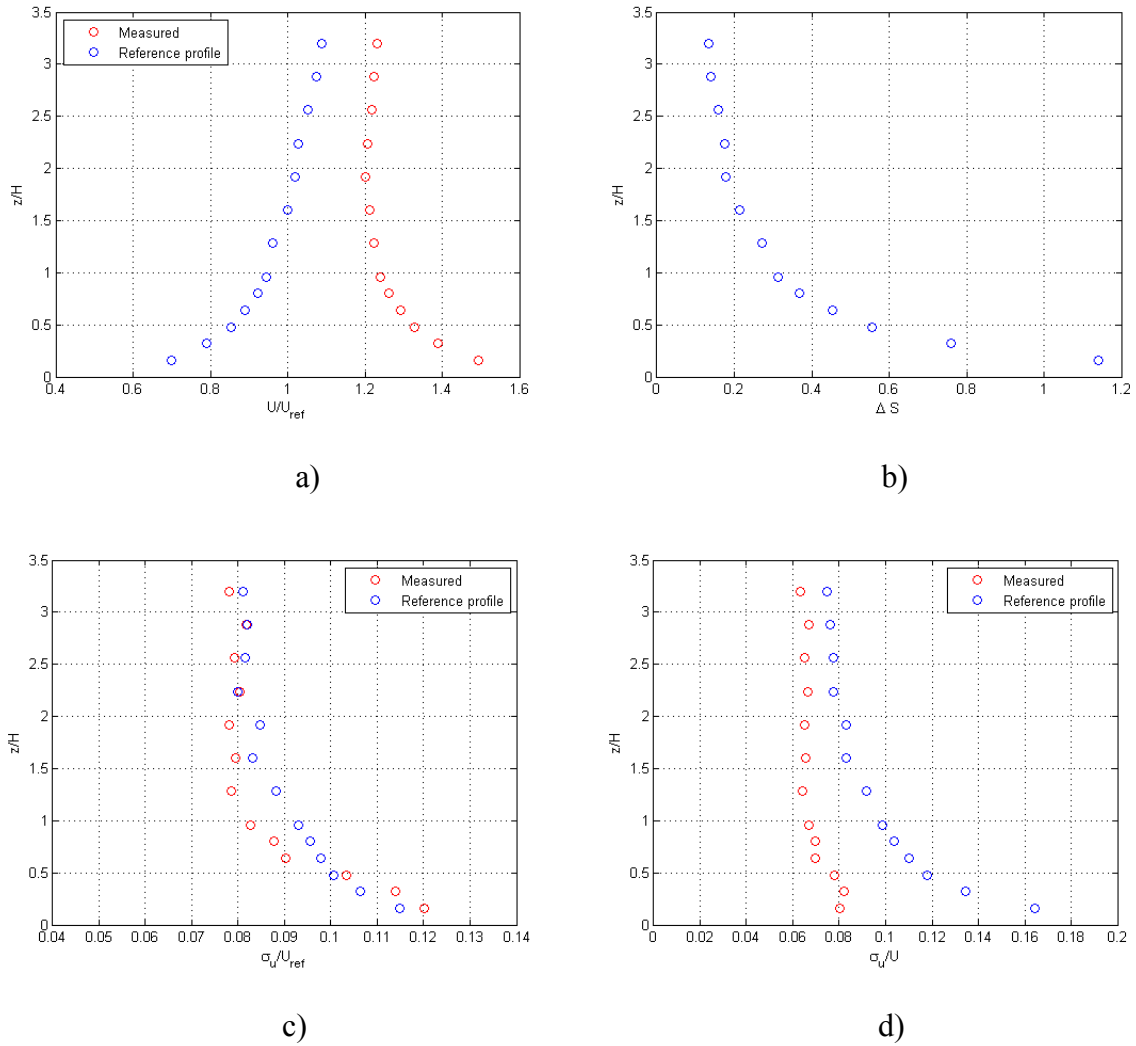


Figure 28: a) Mean horizontal velocity profile compared with the reference profile. b) Fractional speed-up (ΔS). c) The normalized standard deviation compared with the reference profile. d) Turbulence intensity compared with the reference profile.

8.3.2.1 Velocity and fractional speed-up

Figure 27a shows the mean horizontal velocity at the hill peak together with the reference velocity. The difference between the reference and measured velocity is better displayed in Figure 27b.

Paul Carpenter et. al [8] measured a ΔS_{max} of 1.08 near the surface at the peak of a steep sinusoidal hill and Kjersti Røkenes et. al. [35] observed a ΔS of approximately 0.6 at $z/H = 0.16$ for a hill peak shaped as a Gaussian probability density function.

Figure 16 has a ΔS_{max} of 1.14 at $z/H = 0.16$. A higher ΔS was expected in this experiment because of a larger mean angle of the hill. The value of ΔS in Case 2, follows the same trend as in Case 1. In the region between the surface and $z/H = 1.6$, decreases ΔS rapidly before it becomes close to constant at the height $z/H = 1.6$.

The blockage will also in this case lead to an increase in the mean horizontal velocity. Stig Sund observed that it is expected an increase of 5% in the mean horizontal velocity because of the model blockage [37].

8.3.2.2 Turbulence intensity

The results in figure 27c show a small increase in the normalized standard deviation compared to the reference profile in the region $z/H=0.16$ to $z/H = 0.48$. In the region $z/H=0.5$ to $z/H=1.44$ the measured values are lower compared to the reference value. Above this point, the difference between the measured values and the reference values are small.

If 0° is the leading edge of the hill (half-cylinder) and 90° is the hill peak, then from the leading edge and to approximately 75° , the flow over the cylinder has a favourable pressure gradient [37]. Because of the favourable pressure gradient the flow is accelerated and the normalized standard deviation decreases near the wall. In the region between 75° and 90° , it is an adverse pressure gradient which will decelerate the flow and decrease the normalized standard deviation near the wall. This may be the reason for the regions with higher and lower normalized standard deviation compared to the reference profile.

The turbulence intensity in figure 27d above the hill peak is considerably more uniform over the boundary layer compared to the reference profile. A similar trend was also observed in case 1. The reason for this is mainly the increase in the mean horizontal velocity near the surface where the largest normalized standard deviations are found, but also because of a decrease in the normalized standard deviation in the region $z/H=0.5$ to $z/H=1.44$.

8.3.3 Comparison with Norwegian Standard

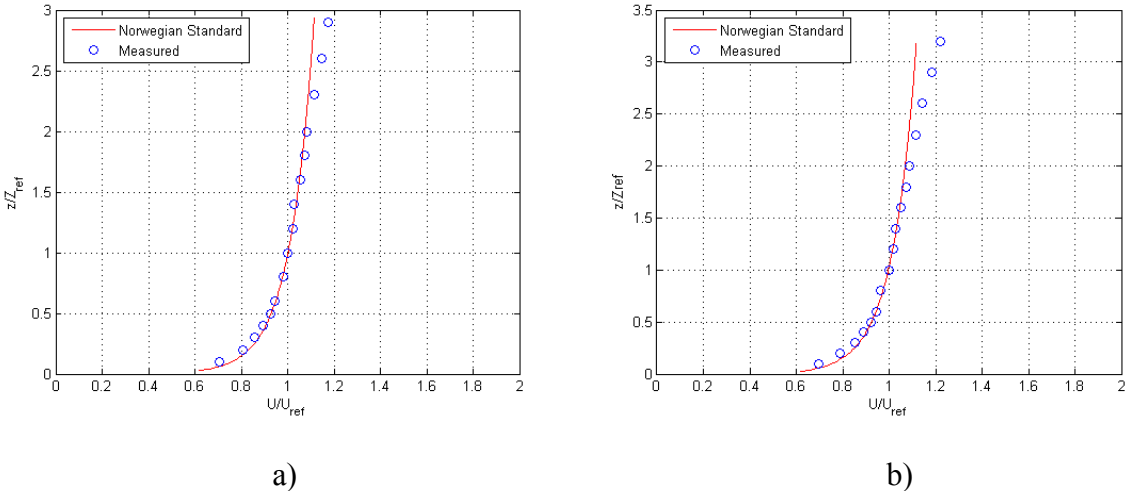


Figure 29: On set profile for case 1 a) and for case 2 b), compared with the profile law proposed in the Norwegian standard to represent the ABL.

Norwegian standard gives a good approximation for the on-set profile. The proposed law which is used in order of the power-law fits well in its flat terrain mode when constants

are adjusted. Like in figure 16 this law gives a good fitting up to a value of 1 in height or a value of 2 in figure 28 (this is due to the two different z_{ref} used in the plot).

8.3.3.1 Profile comparison results

The Norwegian Standard (described in chapter 5) has a topography factor which was developed to help construction engineers to estimate the horizontal mean velocity speed-up over hills and escarpments. Wind tunnel results were compared with the “Norwegian Standard” for the escarpment and hill. The two different cases are the same as in section 8.3 with the same reference values (U_{ref} , Z_{ref} and H) and inflow conditions. The wind tunnel experiments were scaled up by 800 in case 1 and 750 in case 2.

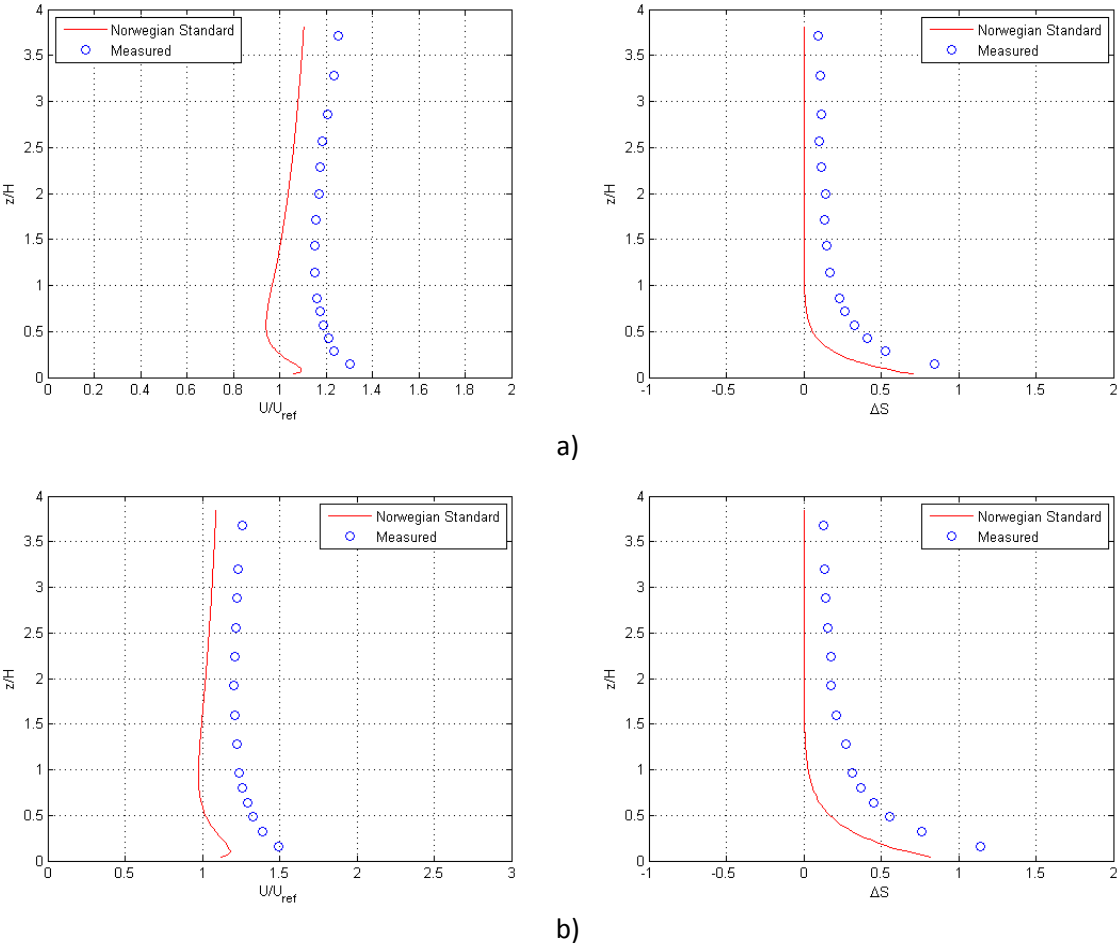


Figure 30: Mean horizontal velocity profile compared with the reference profile and fractional speed-up (ΔS) for; a) case 1 and b) case 2.

8.3.3.2 Discussion

The figures show the same trend when the estimated horizontal mean velocity profile obtained from the “Norwegian Standard” are compared with the scaled up results observed in the wind tunnel experiments. The Norwegian standard underestimates the horizontal mean velocity at the escarpment crests in case 1 and above the hill peak in case 2, compared with the scaled-up wind tunnel results. In previous experiments have the same trend has been

observed when similar types of building standards have been compared with model and field tests [5].

An increase in mean velocity for the wind tunnel experiment is expected because of the blockage that models induce in the working section, which will lead to a difference compared to the Norwegian Standard [34]. Another reason for the different results between the Norwegian Standard and the scaled-up wind tunnel experiment may be the fact that the code has a very simplified description of the hill/escarpment shape. Model experiments in wind tunnel show that the horizontal mean velocity profile over hills and escarpments are relatively sensitive to small changes in the hill/escarpment shape and roughness [5].

8.3.4 Comparison with potential flow

For the comparison with the case 1 and case 2, basic potential flow theory is going to be used. Using a direct solution for the case 2 and a numerical solution for the case 1.

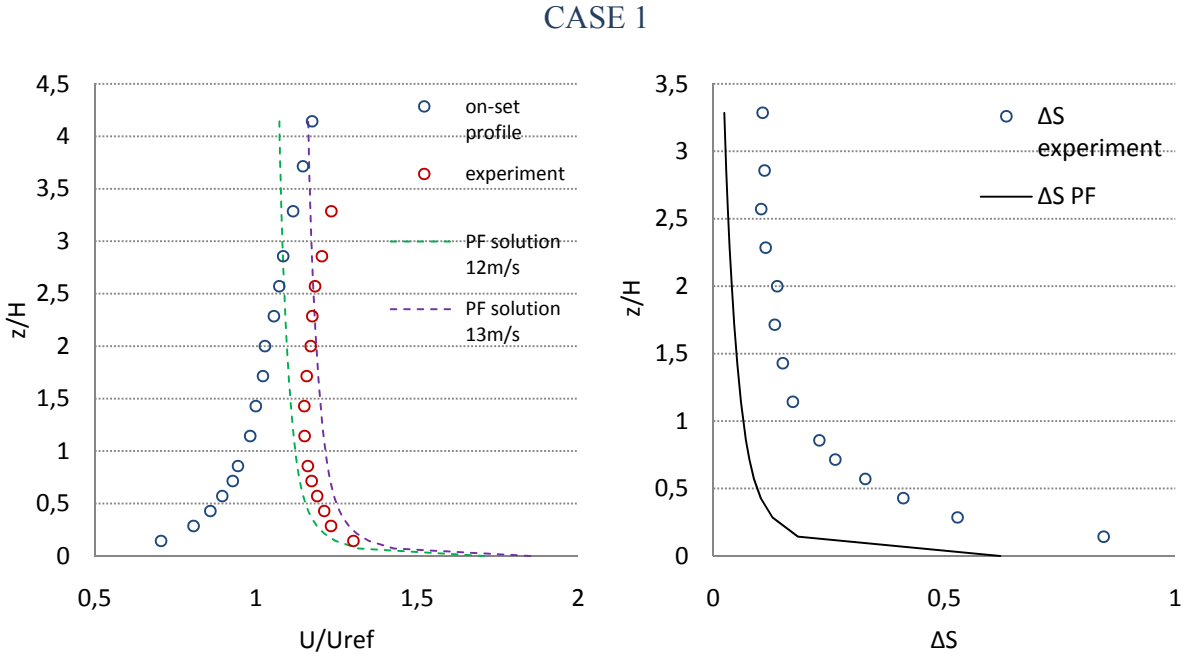
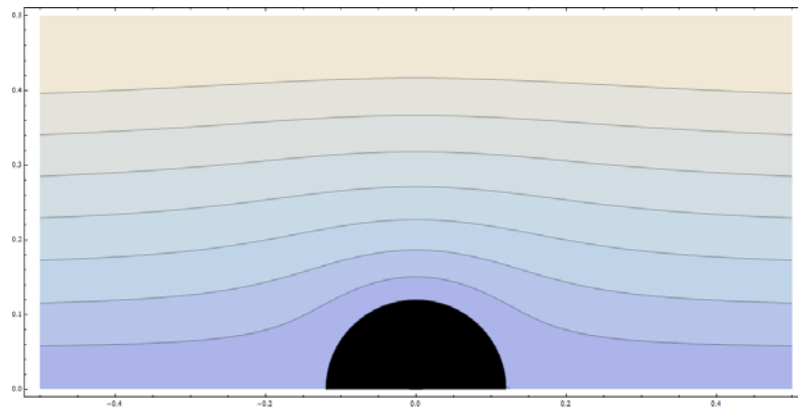


Figure 31: Mean horizontal velocity profile compared with the reference profile and fractional speed-up (ΔS) for case 1.

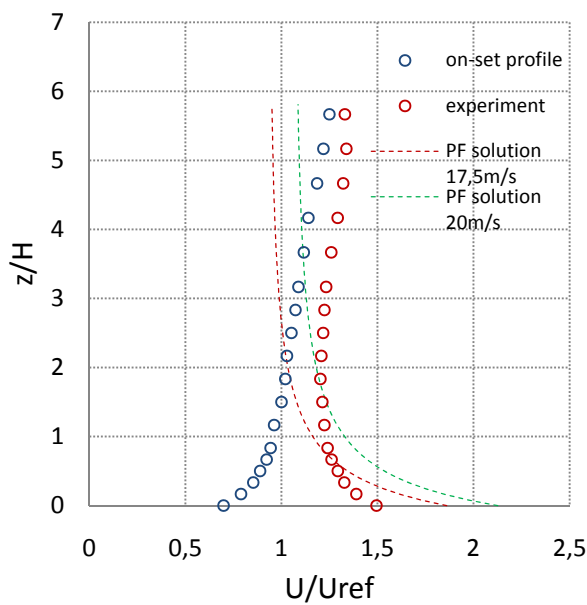
The velocity solution gives a good approximation although it has the same problem as the solution for the cylinder; it has a flat profile boundary condition, so presumably will underestimate the speed up ratio.

The drawback on this theoretical solution is in this case of the speed-up ratio, which clearly gives lower values than the experienced in the wind tunnel, the same tendency of underestimating the speed up that is shown in the section 8.3.3.

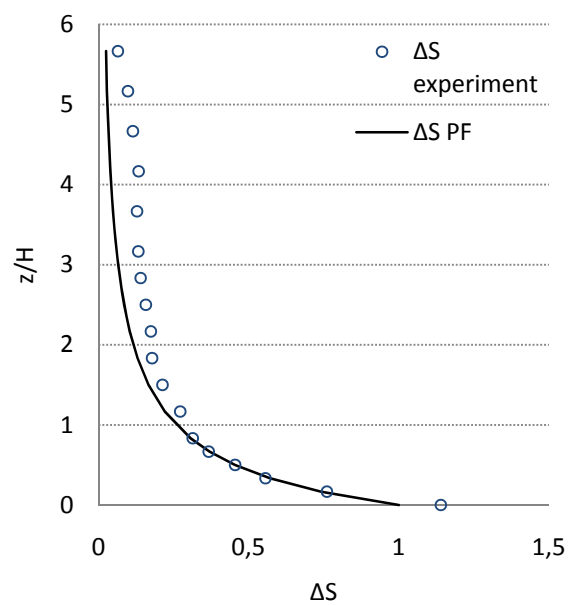
CASE 2: the hill



a)



b)



c)

Figure 32: a) Streamlines of the flow over the cylinder. b) On-set profile compared to the profile over the cylinder and two potential flow solutions. c) Speed-up ratio of the experiment and the potential flow solution. Where $H=62\text{mm}$ is the radius of the cylinder and $U_{ref}=11.3813\text{m/s}$.

It does not give a good fitting when velocity is plotted; this is due to the boundary conditions in the potential flow solution which is a flat profile. That is the reason of the solution to have a higher velocity near the top of the cylinder, with the boundary layer the velocity of the on-set profile is lower at the bottom.

On the other hand the results in terms of speed-up ratio are satisfying, and the results have a good fit with the theoretical potential flow solution.

It has to be said that the discrepancy of the experimental results with the theoretical data might have been influenced by the difficulty to locate the anemometer in the very top of the

cylinder, which on the other hand is easy to get the data for that point in the potential flow solution, so there is a range of uncertainty in the exact relative location of the anemometer to the cylinder. In addition, the blockage effect induced in the working section will also increase the measured velocities in cases 1 and 2.

8.3.5 Pitot and hot wire disagreement

During the simulations over the cylinder a discrepancy between Pitot and hot wire measurements arose. Earlier while the ABL set up time both anemometers match to the perfection at the time of measuring the velocity profile but when measuring the velocities over the cylinder they started to differ one from the other. The discrepancy in the velocity takes place in the sensitive area of a small section just over the top of the cylinder, the disagreement goes from the top of the cylinder up to about 60mm over it. This length matches with the radius of the cylinder (62mm).

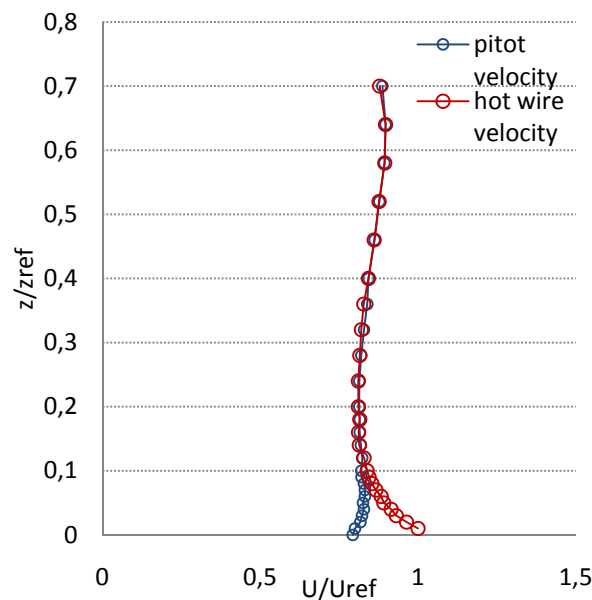


Figure 33: Pitot and hot wire disagreement.

First of all it was thought to be a problem of layer separation that was not constant along the length of the cylinder, which means the separation occurred at different angles relative to the cylinder. By that assumption the Pitot could have been submerged in a fully turbulent flow after the separation from the cylinder while the hot wire could not.

It was decided to switch measuring positions of the hot wire and the Pitot, in a way that Pitot would be measuring at the same point that the hot wire was measuring and vice versa. The results of this were the same profiles as before, no changes. Also the position of the two anemometers was changed and put 20mm further forward, the aim was to measure before the separation occur, but same results were achieved

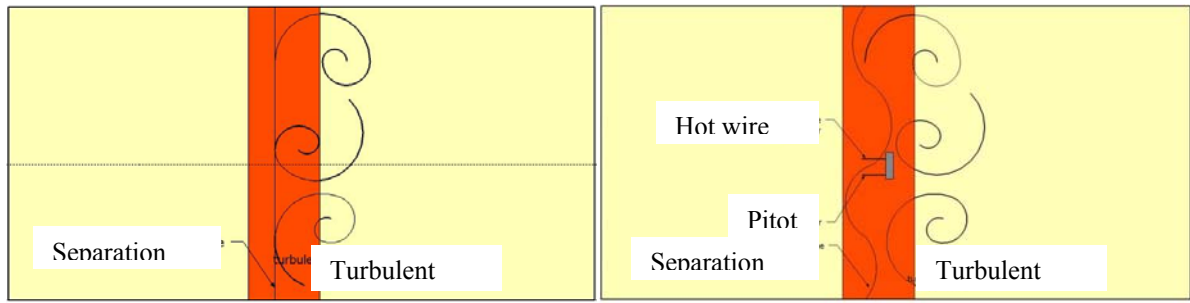


Figure 34: Separation line of the cylinder.

In the second attempt, the problem was thought to be the velocity to be composed of a horizontal and vertical component. To validate this hypothesis the hot wire was rotated 90° over its longitudinal axis. In this way if the flow had a vertical component the values of the measurements with the hot wire rotated were going to be smaller than before. But again the results were identical, by the way this shows that the flow is completely horizontal over the cylinder and that the assumptions of the potential flow theory of a zero vertical component of the velocity are close to reality.

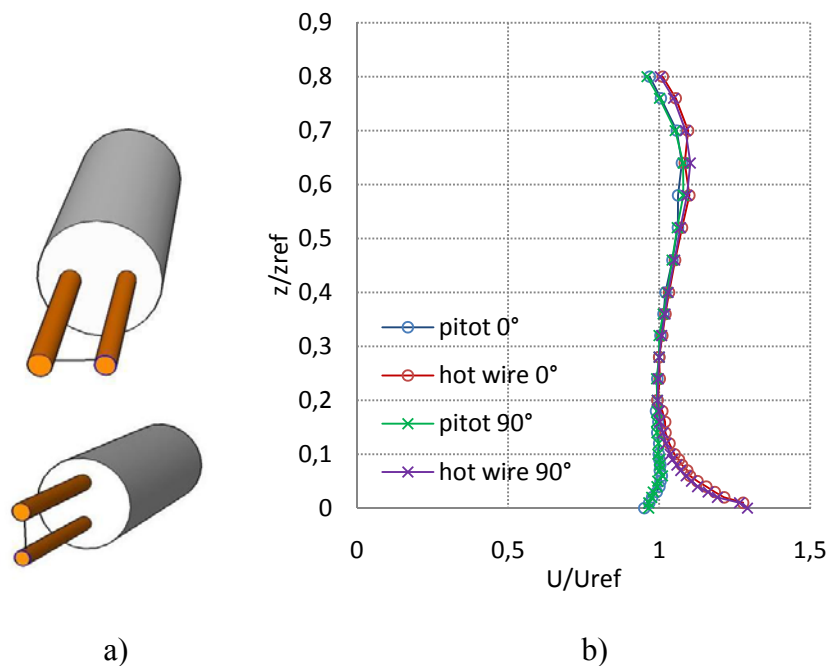


Figure 35: a) Hot wire in 0° and 90° configurations. b) mean velocity profile.

The last possible issue that was thought to might be the cause was that the two pressures measured by the Pitot were not measured at the same point, in fact the static pressure hole is a couple of centimetres downwind the total pressure hole. So the hypothesis was that between the two holes flow conditions and the static pressure was affected by some flow coming through the static pressure hole.

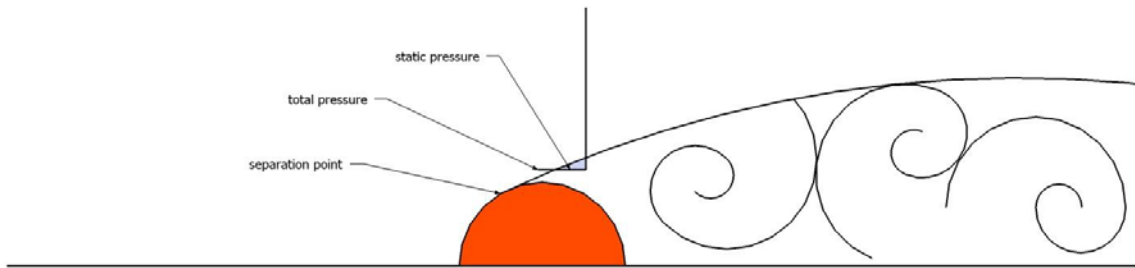


Figure 36: representation of the wake downwind the cylinder.

To avoid this difference of relative positioning it was done a measurement of the profile using only the total pressure leaving the other inlet pressure to the atmospheric pressure in the laboratory. Then the Pitot was moved forward, so that the static pressure was now measured at the same point that was measured before the total pressure. The other pressure inlet was left to ambience pressure as before.

The velocity calculation did not deserve more difficulty than before, by this way both static pressure and total pressure were measured as a difference between ambience pressure and the pressure of the Pitot, it was assumed that the ambience pressure did not change between the two experiments. So by doing this it was possible to measure the velocity profile with the Pitot without the uncertainty that the conditions might change between the two holes.

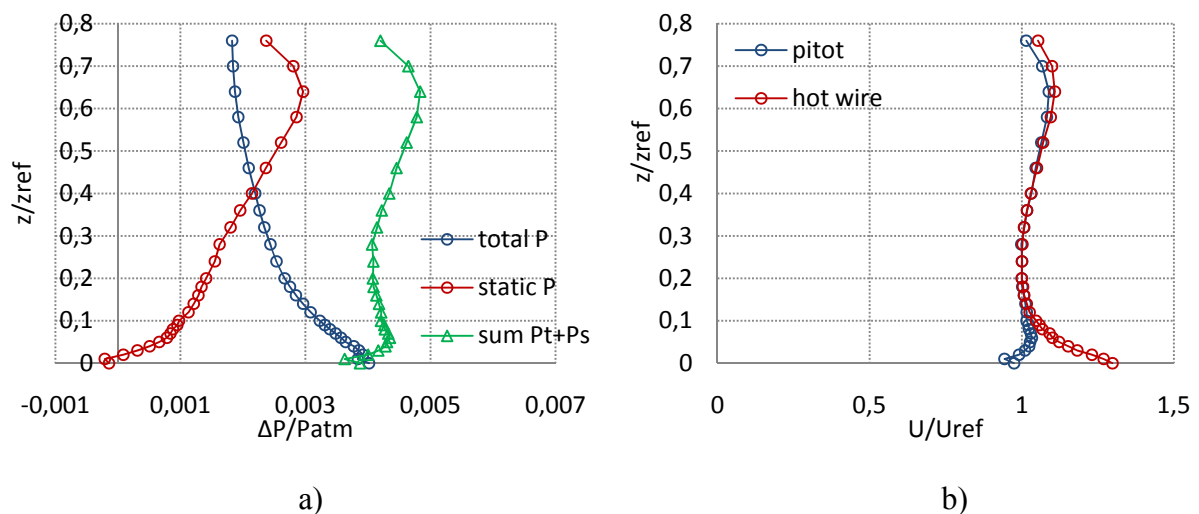


Figure 37: a) Measured Pitot pressures. b) mean velocity profile.

The results show once again the same disagreement in the lowest part of the profile.

The principle of Pitot and hot wire velocity estimation is completely different, while the Pitot simply estimates the velocity from the difference of static and total pressure; the hot wire is non-dependant of the pressure, but on the temperature to estimate the velocity.

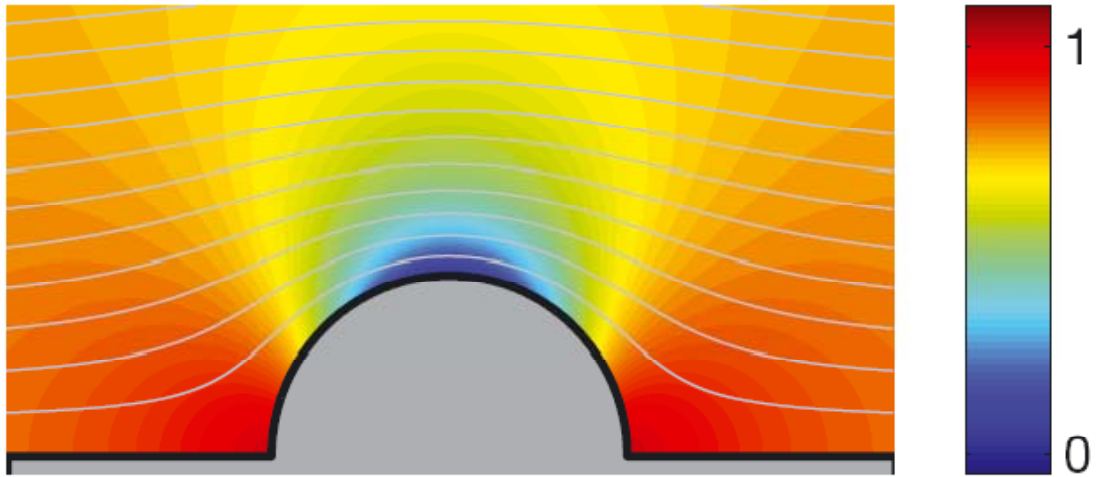


Figure 38: Pressure field form potential flow solution [43].

So all things taken into account, the problem might be found in the adverse pressure gradient formed over the top of the cylinder, and that phenomenon in addition to the fact that the Pitot estimation of velocity is based on the pressure difference.

CHAPTER 9

9 Conclusions

A wind tunnel study of speed effects above the very crest of a sharp-edged escarpment and a hill peak in a simulated atmospheric boundary layer has been carried out. The mean horizontal velocity profiles obtained in the wind tunnel experiment were also compared with the Norwegian Standard and potential flow theory.

- **Simulated boundary layer:**

Two part-depth atmospheric boundary layer simulations using the modified Counihan method are presented.

The simulated atmospheric boundary layer's longitudinal parameters agreed well with full scale data for the mean velocity profiles, power spectrum of velocity fluctuations and integral length scales of velocity fluctuations.

The turbulence intensity was below the desired value and was the only flow parameter that disagreed when compared with full scale data. Scale ratios of 1:800 and 1:750 were calculated for the simulated boundary layer and it fitted well for the power-law with an exponent of 0.12.

- **Investigation of the speed-up effects:**

The flow above the very crest of a sharp-edged escarpment and the hill peak was compared with the undisturbed up-stream flow for the two cases.

It was observed a decrease in turbulence intensity and a considerably more uniform turbulence intensity profiles with height, compared with the reference profiles.

The mean horizontal velocity profiles above the crest/peak increased in a large proportion at the lowest part of the flow.

As expected was the maximum fractional speed-up ΔS , found at the lowest measurement point above the escarpment crests and hill peak.

- **The Norwegian standard:**

The scaled-up wind tunnel measurements for the escarpment and hill were compared with horizontal mean velocity estimations from the Norwegian Standard.

It was observed that the Norwegian Standard estimated lower horizontal mean velocity speed profiles than observed in the wind tunnel experiment for the two cases.

- **Potential flow:**

The comparison between potential flow solutions for the flow over a cylinder shows a good agreement of fractional speed-up ΔS , however an expected disagreement with the horizontal velocity profile was observed. This was due to the fact that potential

flow theory uses a flat uniform velocity profile as boundary condition and at the wind tunnel is used an ABL velocity profile.

The solution for the ramp totally underestimates the speed-up ratio as the Norwegian Standard does too.

- **The use of hot wire instead of Pitot tube**

The use of the Pitot tube for measuring the velocity profile over cylinders leads to an error, it has been deduced that the reason of this should be the adverse pressure gradient formed on the very top of the cylinder. On this research it has been concluded that the use of a hot wire gives a valid result with a good approach to the theoretical potential flow solution.

CHAPTER 10

10 References

- [1] Arya, S.P.S., M.E. Capuano and L.C. Fagen. (1987), “Some fluid modeling studies of flow and dispersion over two-dimensional low hills”. *Atmospheric Environment* (1967) Volume 21, Issue 4, 1987, Pages 753-764. [23]-
- [2] Balendra, T., D.A. Shah, K.L. Tey and S.K Kong. (2002), “Evaluation of flow characteristics in the NUS-HDB Wind Tunnel”. *Journal of Wind Engineering and Industrial Aerodynamics*, Volume 90, Issue 6, June 2002, Pages 675-688 [7]-
- [3] Bertin, John J. and Russel M. Cummings. (2008), *Aerodynamics for engineers*. Prentice Hall, 5th edition. Pages 92-96 [36]-
- [4] Bortoli, M.E. de, B. Natalini, M.J. Paluch and M. B. Natalini. (2002), “*Part-depth wind* tunnel simulations of the atmospheric boundary layer”. *Journal of Wind Engineering and Industrial Aerodynamics*, Volume 90, Issues 4-5, May 2002, Pages 281-291[33]-
- [5] Bowen, A.J and D. Lindley. (1976), “A Wind-Tunnel Investigation of the Wind Speed and Turbulence Characteristics Close to the Ground Over Various Escarpment Shapes”. *Boundary-Layer Meteorology*, Volume 12, Number 3 (October 1977). [21]-
- [6] BS EN 1991-1-4: Eurocode 1: Actions on structures. General actions – Wind actions. [30]-
- [7] Burton, T., D. Sharpe, N. Jenkins and E. Bossanvi. (2001), *Wind energy handbook*, Wiley. [27]-
- [8] Carpenter, Paul and Nicholas Locke. (1999), “Investigation of wind speeds over multiple two-dimensional hills”. *Journal of Wind Engineering and Industrial Aerodynamics* Volume 83, Issues 1-3, November 1999, Pages 109-120[24]-
- [9] Cermak, J.E. (1970), “Air motion in and near cities – determination by laboratory simulation”. College of Engineering, Colorado State University, Fort Collins, CO[39]-
- [10] Cermak, J.E. (1971), “Laboratory simulation of the atmospheric boundary layer”. *AIAA Journal*. Volume 9, Issue 9, September 1971, Pages 1746-1754 [38]-
- [11] Cermak, J.E. (1973), “Physical Modelling of Atmospheric Flow for Air Pollution Studies”. ASME, Flow Stud in Air and Water Pollut, Jt Meet; Atlanta, GA, USA; 20 June 1973 through 22 June 1973. [4]-
- [12] Cermak, J.E.. “Wind-Tunnel Simulation of Atmospheric Flow and Dispersion”. [1]-
- [13] Chaudhry, F.H and J.E Cermak, ”Simulation of Flow and Diffusion Over an Urban Complex”. [6]-
- [14] Cook, N. J.. (1997), “*The Deaves and Harris ABL model applied to heterogeneous terrain*”. *Journal of Wind Engineering and Industrial Aerodynamics*, Volume 66, Issue 3, March 1997, Pages 197-214 [29]-

- [15] Cook, N.J. (1973), “On simulating the lower third of the urban adiabatic boundary layer in a wind tunnel”. *Atmospheric Environment*. Volume 7, Issue 7, July 1973, Pages 691-705 [43]-
- [16] Cook, N.J. (1977), “Determination of the Model Scale-factor in Wind-Tunnel Simulations of the Adiabatic Atmospheric boundary layer”. *Journal of Industrial Aerodynamics* Volume 2, Issue 4, January 1978, Pages 311-321 [9]-
- [17] Cook, N.J.. (1978), “Wind-Tunnel Simulation of the Adiabatic Atmospheric Boundary Layer by Roughness, Barrier and Mixing Methods”. *Journal of Industrial Aerodynamics*, Volume 3, Issue 2-3, 1978, Pages 157-176 [11]-
- [18] Counihan, J.. (1968), “An Improved Method of Simulating an Atmospheric Boundary Layer in a Wind Tunnel”. *Atmospheric Environment* (1967), Volume 3, Issue 2, March 1969, Pages 197-200, IN1-IN2, 201-214 [12]-
- [19] Counihan, J.. (1975), “Adiabatic atmospheric boundary layers: a review and analysis of data from the period 1880-1972*”. *Atmospheric Environment*, Volume 9, Issue 10, 1975, Pages 871-905[28]-
- [20] Doebelin, Ernest O.. (2004). *Measurement systems*, McGraw Hill, 5th edition. [25]-
- [21] Dyrbye, Claes and Svend O. Hansen. (1997), *Wind loads on structures*, Wiley. [8]-
- [22] Farrell, Cesar, Arun K.S. Iyengar. (1999), “Experiments on the wind tunnel simulation of atmospheric boundary layers”. *Journal of Wind Engineering and Industrial Aerodynamics* Volume 79, Issue 1-2, 1 January 1999, Pages 11-35 [40]-
- [23] Ferreira A.D., A.M.G. Lopes, D.X. Viegas and A.C.M. Sousa. (1995), “Experimental and numerical simulation of flow around two-dimensional hills”. *Journal of Wind Engineering and Industrial Aerodynamics* 54/55 (1995) 173-181[19]-
- [24] Garret, J.R. (1992), *The Atmospheric Boundary layer*. Cambridge Univ. Press, Cambridge. [2]-
- [25] Irwin, H.P.A.H.. (1980), “The Design of Spires for Wind Simulation”. *Journal of Wind Engineering and Industrial Aerodynamics*, Volume 7, Issue 3, May 1981, Pages 361-366 [13]-
- [26] Ishibara T., Hibi K. and Oikawa S. (1999), “A wind tunnel study of turbulent flow over a three-dimensional steep hill”. *Journal of Wind Engineering and Industrial Aerodynamics* Volume 83, November 1999, Pages 95-107
- [27] Johnson, Richard W.. (1998), *The handbook of fluid dynamics*, CRC Press. [18]-
- [28] Kozmar, Hrvoje. (2008), “Influence of spacing between buildings on wind characteristics above rural and suburban spires”. [14]-
- [29] Kozmar, Hrvoje. (2009), “*Natural wind simulation in the TUM boundary layer wind tunnel*”. EACWE 5. Florence, Italy, 19th – 23rd July 2009[32]-
- [30] Kozmar, Hrvoje. (2009), “Scale effects in wind tunnel modeling of an urban atmospheric boundary layer”. *Theoretical and Applied Climatology*, Volume 100, Issue 1, February 2010, Pages 153-162 [3]-
- [31] Lopes, M.F.P, M.Glória Gomes and Joao G. Ferreira. (2008), “Simulation of the atmospheric boundary layer for model testing in a short wind tunnel”. *Experimental Techniques*. Volume 32 Issue 4, Pages 36 – 43[42]-

- [32] Manwell, J.F, J.G. McGowan and A.L. Rogers. (2002), *Wind Energy Explained*, Wiley[10]-
- [33] Nagano, Y., Tsuji T., Houra T. (1998), “Structure of turbulent boundary layer subjected to adverse pressure gradient”. *International Journal of Heat and Fluid Flow*, 19 (5), pp. 563-572. [15]-
- [34] NS 3491-4: Norwegian standard[37]-
- [35] Røkenes, Kjersti and Per-Åge Krogstad. (2009), “Wind tunnel Simulation of Terrain Effects on Wind Farm Siting”. *Wind Energy*, Volume 12, Issue 4, Pages 391 - 410[20]-
- [36] Snyder, William H. and Ian P. Castro. (2002), ”The critical Reynolds number for rough-wall boundary layers”. *Journal of Wind Engineering and Industrial Aerodynamics* Volume 90, Issue 1, January 2002, Pages 41-54[5]-
- [37] Sund, Stig. (2010), “Effect of blockage on high Reynolds Number flow over a semi-circular floor mounted obstacle in a rectangular wind tunnel” [17]-
- [38] Tieleman, H.W. and Timothy A. Reinhold. (1978), “On the wind-tunnel simulation of the atmospheric surface layer for the study of wind loads on low-rise buildings”. *Journal of Industrial Aerodynamics*. Volume 3, Issue 1, 1978, Pages 21-38[41]-
- [39] White, B.R.. (1996), “Physical modelling of atmospheric flow and environmental applications”. [26]-
- [40] White, Frank M.. (1991), *Viscous Fluid Flow*. McGraw-Hill Science/Engineering/Math; 2nd edition. [22]-
- [41] White, Frank M.. (1998). *Fluid mechanics*. Mcgraw-Hill College, 4th edition. Pages 495-510. [34]-
- [42] Wieringa, J., A.G. Davenport, C. Sue. B. Grimmond and Tim. R. Oke. (1992), “New revisioin of Davenport roughness classification”. *Journal of Wind Engineering and Industrial Aerodynamics*. Volume 41, Issues 1-3, October 1992, Pages 357-368[31]-
- [43] Turnbull B. and MvElwaine J.N. (2010), “Potential flow models of suspension current air pressure”. *Annals of Glaciology* 51(54) 2010.

Appendix

A.1 Wind Tunnel Results

It was also done a wind tunnel experiment on flow above the very crest of two more escarpments. It was a mistake because the two models were only 0.4m wide and the wind tunnel was 1 m wide.

Because of this, end effects could influence the results and the flow could not be considered as two-dimensional. It was decided to present the results since it can be assumed that the cross-flows were weak in the center of the hill where the measurements were done [40]. The inflow conditions were the same as for the escarpment in case 1. The dimensions of the escarpments were in case 3 $L = 0.1\text{m}$ and $H = 0.058\text{m}$ and in case 4 $L = 0.069\text{m}$ and $H = 0.058\text{m}$.

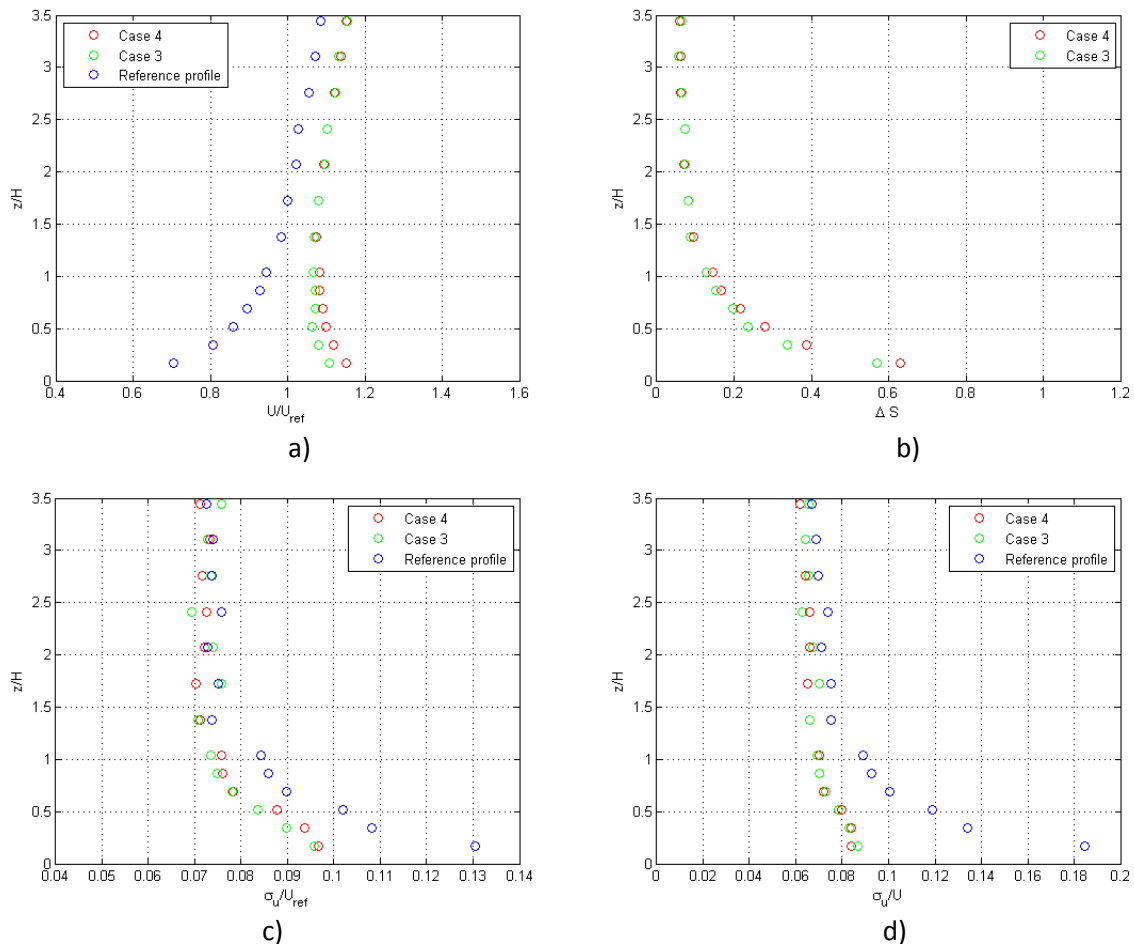


Figure 39: The results for case 3 and 4; a) Mean horizontal velocity profile compared with the reference profile. b) Fractional speed-up (ΔS). c) The normalized standard deviation compared with the reference profile. d) Turbulence intensity compared with the reference profile.

In figure 38a is the mean horizontal velocity profile above the very crest shown for case 3 and 4 compared with the reference profile. The fractional velocities for both cases are also shown in figure 38b.

The fractional speed-ups have the same trend as in case 1, but the size of the speed-up varies between the different escarpments.

Arya et. al. [1] and Røkenes et. al. [35] observed that the fractional speed-up was strongly influenced by the slope of the escarpment or hill. The same result can be observed in figure 38b. The results show that the largest maximum fractional speed-up is found in case 4 ($\Delta S=0.63$) which have a steeper slope than case 3 ($\Delta S=0.57$).

The normalized standard deviation standard deviations in figure 38c show the same trend as in case 1 when it is below the reference profile near the surface but becomes equal higher up. A possible reason for this decrease was mentioned in the discussion of case 1.

Figure 38d shows that the turbulence intensity decreases compared to the reference profile also in case 3 and 4. The reason is the decrease in normalized standard deviation near the surface and an increase in the mean horizontal velocity.

A.2 The wind tunnel results compared with the Norwegian Standard

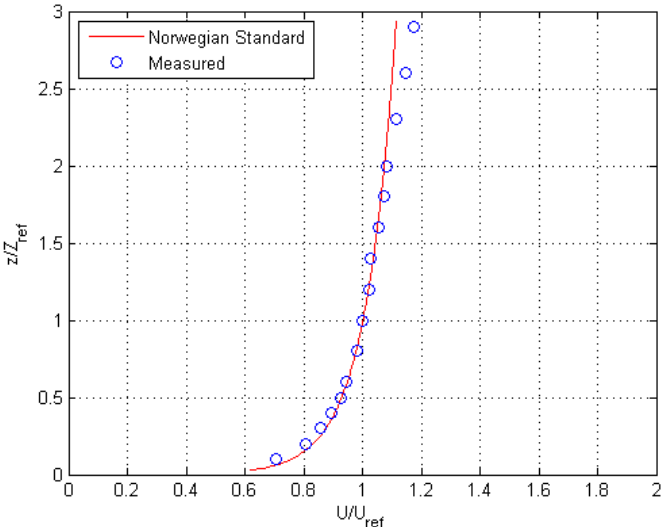


Figure 40: Measured undisturbed mean velocity profile compared with the Norwegian Standard.

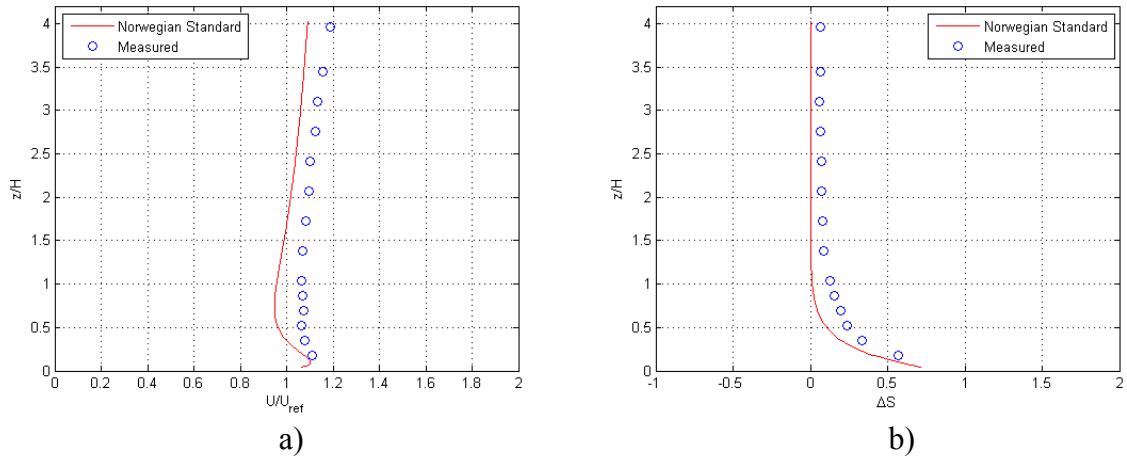


Figure 41: Case 3 compared with the “Norwegian Standard” for; a) the mean horizontal velocity at the hill peak, b) the fractional speed-up

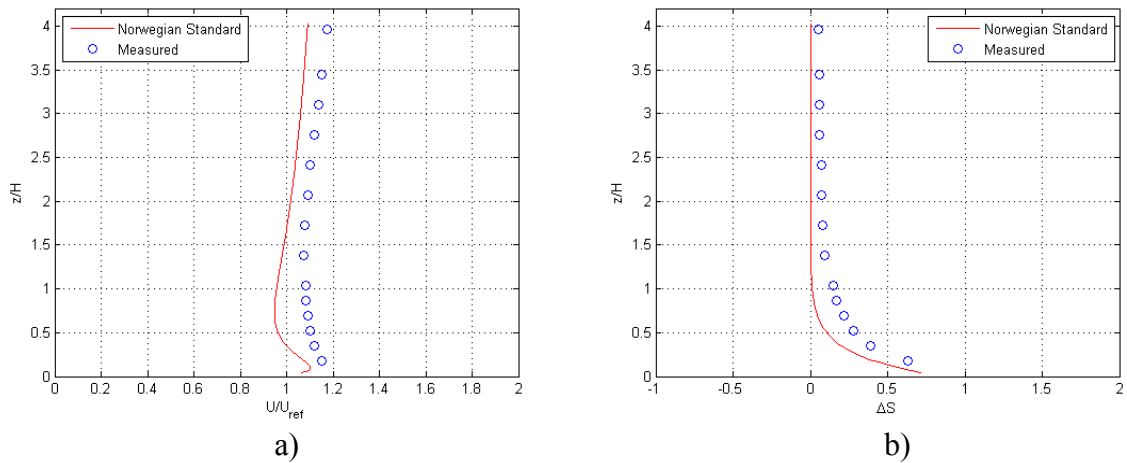


Figure 42: Case 4 compared with the “Norwegian Standard” for; a) the mean horizontal velocity at the hill peak, b) the fractional speed-up

When the scaled-up mean horizontal velocity profiles from the wind tunnel experiment are compared with estimated results obtained from the “Norwegian Standard” the same trend as for the hill (case 2) and the escarpment (case 1) can be observed. The horizontal mean velocity profile results from the Norwegian Standard gives a lower estimate compared to the scaled-up wind tunnel measurements.

The results show a better agreement than in case 1 and 2. This may be because of the decrease in blockage ratio of the working section, which was 4.64%.

A.3 The potential flow

CASE 3

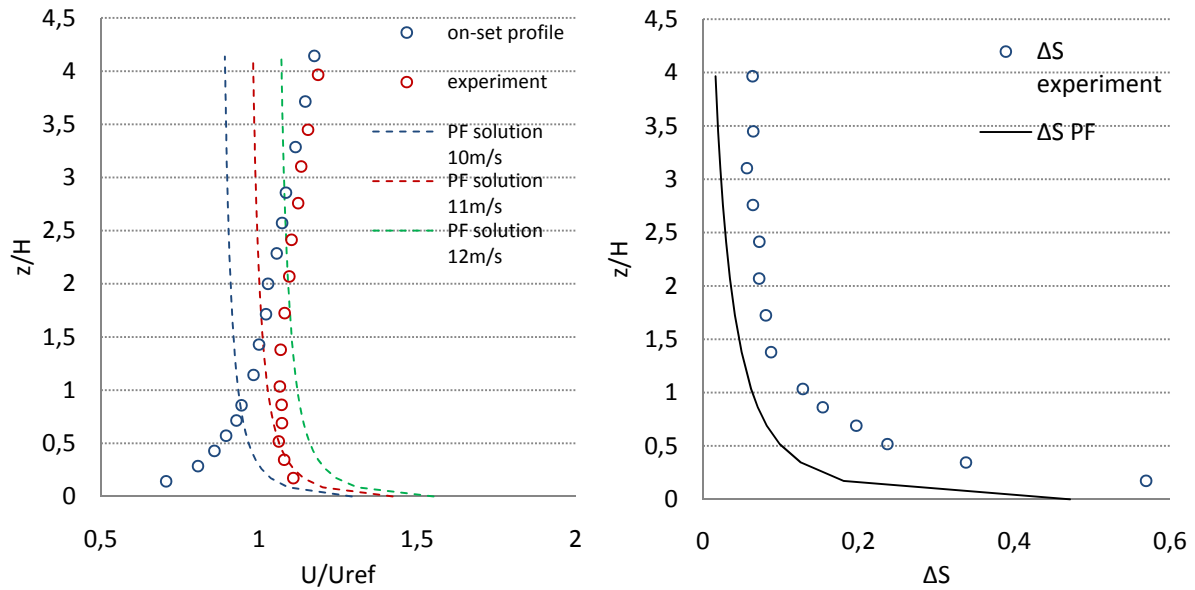


Figure 43: Mean horizontal velocity profile compared with the reference profile and fractional speed-up (ΔS) for case 3.

In figure 42 is represented the flow over the ramp with the smallest angle 30° . This ramp gives better approximation in both, velocity and speed up ratio, than case 1. Still the potential flow solution is far from close to the experimental data.

CASE 4

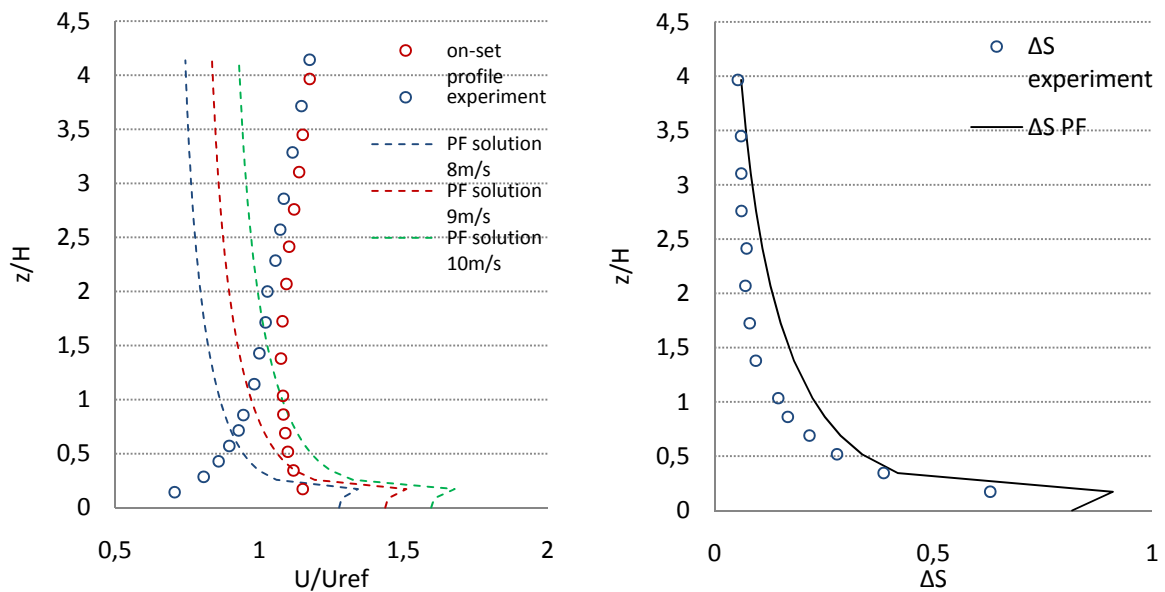


Figure 44 : Mean horizontal velocity profile compared with the reference profile and fractional speed-up (ΔS) for case 4.

In case 4, with an angle of 40° the potential flow solution approximates to the experimental data in the speed-up ratio, but not in the velocity prediction. Indeed in this case the speed-up ratio is higher in the potential flow solution than in the experimental results, but it shows an overall good fit.

The sudden decrease of velocity when approximating to the surface in the numerical model could have a mathematical origin.